Facies and architecture of the SCIc formation (Schisto-Calcaire Group), Republic of the Congo, in the Niari-Nyanga and Comba subbasins of the neoproterozoic west Congo basin after the marinoan glaciation event

Anna Perla Ackouala Mfere, Franck Delpomdor, Jean-Noël Proust, Florent Boudzoumou, Yannick y Callec, Alain Préat

HAL Id: insu-02497974
https://insu.hal.science/insu-02497974

Submitted on 4 Mar 2020

Journal Pre-proof

Facies and architecture of the SCIc formation (Schisto-Calcaire Group), Republic of the Congo, in the Niari-Nyanga and Comba subbasins of the neoproterozoic west Congo basin after the marinoan glaciation event

Anna Perla Ackouala Mfere, Franck Delpomdor, Jean-Noël Proust, Florent Boudzoumou, Yannick Callec, Alain Préat

Please cite this article as: Mfere, A.P.A., Delpomdor, F., Proust, Jean.-Noë., Boudzoumou, F., Callec, Y., Préat, A., Facies and architecture of the SCIc formation (Schisto-Calcaire Group), Republic of the Congo, in the Niari-Nyanga and Comba subbasins of the neoproterozoic west Congo basin after the marinoan glaciation event, *Journal of African Earth Sciences* (2020), doi: https://doi.org/10.1016/j.jafrearsci.2020.103776.

1   **Facies and architecture of the SCIc Formation (Schisto-Calcaire Group), Republic of**

2   **the Congo, in the Niari-Nyanga and Comba subbasins of the Neoproterozoic West**

3   **Congo Basin after the Marinoan glaciation event**

4

5   **Authors:**

6   Anna Perla Ackouala Mfere[1,2]*, Franck Delpomdor[3], Jean-Noël Proust[4], Florent Boudzoumou[2],

7   Yannick Callec[5], Alain Préat[1]

8

9   **Affiliations:**

10 [1]*Université Libre de Bruxelles, Department of Earth Sciences and Environmental Sciences, 50 av. FD*

11 *Roosevelt, B-1050, Brussels, Belgium, Corresponding author: ackouala8@yahoo.fr*

12 [2]*Université Marien Ngouabi, Département de Géologie BP69, Brazzaville, People's Republic of the Congo*

13 [3]*Illinois State Geological Survey, University of Illinois at Urbana-Champaign, 615 E. Peabody Dr, US-61820,*

14 *Champaign, IL, USA*

15 [4] *Univ Rennes, CNRS, UMR6118 Geosciences, 35000 Rennes, France*

16 [5]*Bureau de Recherches Géologiques et Minières, 3 av. Claude Guillemin, BP 36009, F-45060 Orléans,*

17 *Cédex2, France*

18

21

22 **Abstract**

23 The Neoproterozoic Schisto-Calcaire Group (630 to ca. 580 Ma) was deposited on an extensive

24 carbonate shelf in the margin of the Congo Craton in the Niari-Nyanga and Comba subbasins (Gabon

25 and Republic of the Congo). It consists of three carbonate-dominated subgroups (SCI to SCIII, up to

26 1300 m-thick) recording relative sea-level changes. The SCI_c Formation, at the upper part of the SCI

27 Subgroup, is a carbonate succession of meter-scale shallowing-upward cycles, composed of a standard

28 sequence of 7 facies grouped in 5 facies associations recording the evolution of a marine ramp from

29 distal carbonate muds and giant stromatolitic bioherms (F1-F2) and extensive ooid shoals (F3), to

30 proximal settings submitted to evaporation near a sabkha (F7). Fifth-order 'meter-scale' (or

31 elementary parasequences) packages are grouped into fourth-order sequences (parasequence sets),

32 which are not correlative in the whole basin. Two categories of fifth-order elementary parasequences

33 are recognized, on the basis of physical bounding surfaces: (i) subtidal cycles bounded by marine

34 flooding surfaces across which subfacies deepen; and (ii) peritidal cycles bounded by subaerial

35 exposure surfaces. These cycles are the result of the interplay of relative sea-level changes due to

36 eustatic variations related to periodic extensional tectonic events affecting the whole basin. The Niari-

37 Nyanga and Comba subbasins experienced basin tectonics in the general context of the rifting of

38 Rodinia creating changes of relative sea-level in the different parts of the shelf. The SCI_c cycles are

39 enclosed into a third-order sequence with two major transgressive-regressive phases, related to the

40 deposition of the SCI Subgroup. The most typical sedimentologic feature of the SCI_c Formation is the

41 deposition of giant stromatolitic bioherms (stacked up to 20 m) topped by ooid shoals (up to 75 meters

42 thick) deposited during high systems tract prograding and forced regressive systems tract phases that

43 ended with a lowstand systems tract phase with evaporitic and karstic conditions at the top of the SCI_c

44 Formation. The elementary parasequences and parasequence sets are probably the result of the

45 migration of lateral environments related to the variation of the energy in relation to tectonic setting.

46 As a result, a regional sea-level increase is for the first time highlighted in transgressive systems tract

47 phase (composed of microbial induced sedimentary structures Facies) in the lower part of the SCI_c

48 Formation. The third-order succession can be followed more than 100 km in the Republic of the

49 Congo and several hundred meters from South of Gabon to the Lower Congo in the Democratic

50 Republic of the Congo. Tentative detailed sequence stratigraphy correlations between both Congo's

51 highlight the role of tectonics affecting both areas.

52

1. Introduction

54 The Neoproterozoic Era (~1000-540 Ma) was marked by several catastrophic Snowball Earth-type ice

55 ages involving short-lived global climate and eustatic events (Kirchvink, 1992; Hoffman et al., 1998;

56 Hoffman and Schrag, 2002). At least three long-live Neoproterozoic glacioeras (~715-660 Ma

57 Sturtian, ~655-635 Ma Marinoan, and ~583-581 Ma Gaskiers events were widely identified (Young,

58 1995; Wang and Li, 2003; Allen et al., 2004; Deynoux et al., 2006; Hoffman and Li, 2009; Hoffman et

59 al., 2017). Each event was marked by the deposition of diamictites, widely distributed on all

60 continents. The diamictites are commonly overlain in a sharp contact by a cap carbonate unit,

61 interpreted as the result of a sudden switch back to a greenhouse (Hoffman and Schrag, 2002) climate

62 related to increase of atmospheric carbon dioxide due to volcanic degassing (Hoffman and Schrag,

63 2002). This latter event caused a rapid post-glacial marine transgression, and the turning on of the

64 carbonate factory.

65 However, other works have cautioned that diamictites are not unambiguous glacial indicators, but

66 could represent tectonostratigraphic successions formed in tectonically-active rift basins as Rodinia

67 broke apart, thereby demanding caution in directly inferring glacially controlled climatic and eustatic

68 interpretations from such successions (Direen and Jago, 2008; Eyles and Januszczak, 2004; Arnaud

69 and Eyles, 2006; Carto and Eyles, 2012; Delpomdor et al., 2016). In western-central Africa, recent

70 publications have argued that the post-Marinoan carbonate successions record a marine transgression,

71 interconnected with diachronous and regional tectonic processes related to the onset of the pre-

72 collisional magmatic arc in the Araçuaí-West Congo Orogen, dated around 630 Ma, with an orogenic

73 climax around 585-560 Ma (Delpomdor et al., 2016, 2018, 2019).

74 The aim of our paper is to contribute to the debate on the deposition of carbonate successions in

75 western-central Africa, recording a marine transgression after the Marinoan glaciation event. We

76 propose (1) to re-interpret the deposition of the SCI$_c$ Formation in the Niari-Nyanga and Comba

77 subbasins of the Neoproterozoic West Congo Basin (NWCB), located in the Republic of the Congo,

78 and (2) to describe the vertical thickness variations in the cycles and their organization into different

79 sequence orders as a result of tectonic and eustatic mechanisms. A particular interest concerns the

80 hummocky cross-stratification or « HCS » in the oolitic shoals, which is reported for the first time in

81 this stratigraphic unit. It should also be noted that the oolitic shoals are recently intensively used by

82 the cement industry.

83

84 **2. Geological Setting**

85 The research area concerns exposures along 1,300 km of the western margin of the Congo Craton,

86 from southwestern Gabon across the Republic of the Congo (RC) to the western part of the

87 Democratic Republic of the Congo (DRC) to northern Angola (Fig. 1). The Pan-African West Congo

88 Belt (WCB) is part of the Araçuaí-West Congo Orogen (AWCO) formed during the Gondwanaland

89 amalgamation (ca. 550 Ma; Pedrosa-Soares et al., 2008). In RC, the WCB is subdivided into the

90 aulacogen foreland and the Mayombe thrust-and-fold belt domains, which differ in deformation style

91 and metamorphic grade. The foreland domain is composed of weakly to unmetamorphosed rocks

92 unlike those of the thrust-and-fold belt domain. The WCB comprises several Neoproterozoic

93 sedimentary subbasins (Tait et al., 2011; Delpomdor and Préat, 2013; Préat et al., 2011, 2018), here

94 unified as the NWCB, which is now divided from north to south into the Niari-Nyanga, Comba,

95 Lower Congo and North Angola subbasins (Fig. 1). The Niari-Nyanga and Comba subbasins in RC

4

96   are filled with volcano-sedimentary successions of the West Congolian Supergroup (WCS) (Dadet,

97   1969; Alvarez and Maurin, 1991; Thiéblemont et al., 2009; Charles et al., 2015; Affaton et al., 2016;

98   Préat et al., 2018). In RC, the lithostratigraphic terminology of the WCS has been recently modified

99   by Charles et al. (2015) with, from base to top: (i) the rift-related volcano-sedimentary Sounda Group,

100 correlated to the ~1000-930 Ma Nzadi and ~920-910 Ma Tshela/Senke Banza groups (including the

101 Inga-Lufu- and Gangila-type bimodal magmatism) in DRC (Baudet et al., 2013), (ii) the passive-

102 margin Mayombe Group, stratigraphic equivalent to the Sansikwa and Haut-Shiloango subgroups in

103 DRC, (iii) the Niari Group formerly called the "Upper Diamictite", (iv) the shallow marine Schisto-

104 Calcaire Group, stratigraphic equivalent to the Lukala Subgroup in DRC, including a carbonate outer

105 shelf with nearshore barriers and evaporitic lagoons, and (v) the late-orogenic Mpioka Group (Fig. 2).

106 The Sounda Group is subdivided into the Nemba, Kakamoéka and Mvouti subgroups; the Mayombe

107 Group includes the Mossouva, Lower Diamictite and Louila/Bouenza subgroups; the Schisto-Calcaire

108 Group comprises the SCI, SCII and SCIII subgroups (Dadet, 1969; Alvarez and Maurin, 1991;

109 Alvarez, 1995; Préat et al., 2018; Fig. 2).

110

111 **3. Geochronology**

112 The absolute age of the WCB is relatively well constrained. In DRC, the Sansikwa Subgroup, a

113 stratigraphic equivalent to the Mossouva Subgroup of the Mayombe Group in RC, is younger than

114 920-910 Ma (Tack et al., 2001). The Sansikwa Subgroup is intruded by the Sumbi-type dolerite feeder

115 sills and dykes (De Paepe et al., 1975; Kampunzu et al., 1991). U-Pb determinations on baddeleyite

116 single-grains from a dolerite sill yielded a crystallization age of 694 ± 4 Ma (Straathof, 2011), an age

117 younger than the formerly accepted Sturtian age. The Upper Diamictite Formation in DRC

118   (stratigraphic equivalent with the Niari Group in RC) is interlayered with basalts of tholeiitic affinity

119   including the Kimbungu pillows and hyaloclastic breccias. In Gabon, zircons from a tuff in the

120   metasedimentary Louila/Bouenza Subgroup yielded a U-Pb SHRIMP age of ≤ 713 ± 49 Ma

121   (Thiéblemont et al., 2009). Detrital zircon geochronology and provenance analysis of the Lower

122   Diamictite Formation from DRC gave a maximum depositional age of ~700 Ma (Muanza-Kant et al.,

123   2016) constraining the episodic extensional activity recorded on the present-day African side of the

124   AWCO. Detrital U-Pb single-zircon analysis from the basal contact of the upper formation of the

125   Haut-Shiloango Subgroup in DRC, stratigraphically equivalent with the Louila/Bouenza Subgroup,

126   points to a maximum depositional age of ~650 Ma (Frimmel et al., 2006). Carbonates of the

127   uppermost Haut-Shiloango Subgroup were probably deposited around 645 Ma, according to near-

128   primary $^{87}Sr/^{86}Sr$ ratios which are similar to carbonates deposited worldwide during this time interval

129   (Frimmel et al., 2006; Poidevin, 2007). Similarly, carbonates of the CII unit of the Lukala Subgroup in

130   DRC, stratigraphic equivalent with the SCII Schisto-Calcaire Group, were deposited around ~575 Ma

131   (Poidevin, 2007). Regional metamorphism of the WCB is constrained by an Ar-Ar age of 566 ± 42 Ma

132   (Frimmel et al., 2006) in good agreement with the ~585-560 Ma orogenic climax of the AWCO in

133   Brazil (Pedrosa-Soares et al., 2011). Late Pan African tectonics are constrained by an Ar-Ar age of

134   524.6 ± 4.6 Ma on riebeckite in quartz vein in DRC (Tack et al., 2018) and an K-Ar age of 499 ± 19

135   Ma on illite crystallinity analysis from micas in the Mpioka Group (Fullgraf et al., 2015), that is

136   coeval with 540-490 Ma ages obtained in Angola (Monié et al., 2012).

137   The SCI_c has never been dated but is younger than the Niari Group that is overlain by the cap

138   carbonates (SCI_a), and is older than the carbonates of the SCII Subgroup of the Schisto-Calcaire

139   Group (Fig. 2).

140

141 **4. Methodology**

142 Twenty-seven stratigraphic sections were selected in the SCI$_c$ Formation from outcrops along roads,

143 rivers and in the savanna in two key areas of the Niari-Nyanga and Comba subbasins of the NWCB

144 (Fig. 3). The thinnest section is 2 meter-thick and the thickest is 57 meter-thick. Since the sections

145 have been logged and described close to each other, sometimes in places without localities, it has not

146 been possible to name them systematically according to the geographical locations. The 27 sections

147 are named from B to Y (Ackouala Mfere, 2017) with also MAD8016, MAD8018 and MAD8019. The

148 sections A and E belonging to the SCI$_b$ siltstones (Table 1) are not considered here, sections G and

149 MAD8018 are located in active quarries (Sonocc at Loutété), section MAD1016 is located in Bitoto,

150 section MAD8017 is located in an active quarry (Saris quarry, near Nkayi), and section MAD8019 is

151 located near the locality of Zanzo (Fig. 3). The coordinates of the outcrops are summarized in Table 1.

152 Up to 500 samples were collected for petrography and thin section analysis in order to describe facies

153 associations. The carbonate classification terminologies of Dunham (1962), Embry and Klovan

154 (1972), Sibley and Gregg (1987) were employed for the description of components, matrix and

155 cements. The non-skeletal grains (ooids, intraclasts, peloids, aggregate grains, vadoids), sedimentary

156 textures and structures were systematically quantified.

157

158 **5. Facies association and depositional model**

159 The carbonates of the Schisto-Calcaire Group (SCI, SCII and SCIII Subgroups) were described by

160 Préat et al. (2018). In this paper, we focus on the SCI$_c$ Formation that we describe and interpret in

161 terms of depositional environments and sequences.

162   The SCI$_c$ succession contains five facies associations(FA1 to FA5) that are composed of seven facies

163   (F1 to F7) defined by their lithologies, sedimentary structures, textures, fossil contents (microbial

164   mats) and interpreted as deposited in different depositional environments. Facies 3 (F3) is divided into

165   4 sub-types (F3a,b,c,d) due to the presence of ooids in the mentioned sub-types. These largely marine

166   facies associations are described from the deepest to the shallowest settings and are summarized in

167   Table 2. In this paper, ramp terminology was adopted from Burchette and Wright (1992) with (1) the

168   outer-ramp below the storm wave base (SWB) in the offshore; (2) the mid-ramp between the SWB

169   and the fair-weather wave base (FWWB) in the shoreface transition and (3) the inner-ramp above the

170   FWWB including either high energy shoreface environments and back-shoal infratidal to supratidal

171   environments (e.g., muddy lagoon, tidal flats, swamps) in the backshore.

172

173   ***Outer-ramp***

174   *5.1. Facies association 1 (FA1)*

175   <u>Description</u>

176   FA1 is represented by homogeneous clayey and laminar silty mudstone (F1) (Figs. 4A,C). The

177   laminae consist of a subhorizontal, slightly undulating, alternation of light and darker layers of clayey

178   carbonate siltstones and microbial dome-like (< 0.5 mm) or microlenticular (up to 2.5 mm) mudstones

179   respectively (Figs. 4A-C).

180

181   <u>Interpretation</u>

182   FA1 represents Microbial Induced Sedimentary Structures (MISS; *sensu* Noffke, 2010). The absence

183   of ripple marks, hummocky cross-stratification (HCS), erosional remnants, mat chips, mat curls, true

8

184   fenestral fabrics, desiccation cracks and gas domes suggests a quiet and deep environment (40-60 m?)

185   in the photic zone. The environment is typical of the offshore below SWB as for example on the

186   Ordovician continental shelf of the Montagne Noire, France (Noffke, 2000).

187

188   ***Mid-Ramp***

189   *5.2. Facies association 2 (FA2)*

190   FA2 includes giant reefal stromatolites with stromatoclast floatstones (F2) and ooid

191   grainstones (F3a with HCS).

192

193   <u>Description</u>

194   F2 displays a variety of domes, columns and cone-shaped morphologies forming bioherms

195   and/or biostromes (Figs. 5A-B and D). Reefs, ranging in sizes from 1 m up to 10 m, are

196   exposed as isolated bodies or stacked in large complexes. Narrow inter-reef areas between the

197   domes, and more commonly between the columns, are filled with stromatoclast floatstones

198   with centimetric-sized and elongated fragments or breccias. F3a consists of grey colored

199   oolite grainstones/packstones overlying F2. HCS with gently curved and low angle cross-

200   laminations (< 10°) and swaley cross-stratifications (SCS) are associated with F3a (Figs. 6D-

201   G). The oolites, ranging between 400 μm and 650 μm in diameter, are spherical, concentric or

202   composite. Monocrystalline calcite or rosettes of former sulphate minerals often replace the

203   nuclei.

204   <u>Interpretation</u>

205   The giant dome- and cone-shaped stromatolites formed subaqueously in mid-ramp settings

206   (Kromkamp et al., 2007; Perkins et al., 2007). Stromatoclasts suggest wave- and storm-

207   dominated environments. F2 is locally interstratified and overlain by cross-stratified oolite

208   grainstones of facies 3a (see below, Fig. 6H). HCS in the oolite grainstones (details in section

209   6.2.) confirms sedimentation between the SWB and the FWWB. Oolites originally formed in

210   shallow water more likely around 2 m deep (Keith and Zuppann, 1993) have been later

211   removed from inner-ramp to the mid-ramp by wave action. Concentrically laminated oolites

212   attest high-energy shoals. HCS are the result of storm action (Walker and Plint, 1992) in the

213   shoreface transition region between SWB and FWWB (Pedersen, 1985; Bose and Chaudhuri,

214   1990).

215

216   ***Inner-ramp***

217   *5.3. Facies association 3 (FA3)*

218   FA3 includes oolite grainstones/packstones (F3a without HCS), floatstones/packstones (F3b) and

219   (dolo)wackestones/(dolo)packstones-grainstones (F3c).

220

221   <u>Description</u>

222   F3a consists of oolitic grainstones/packstones (Fig. 7A) overlying or interfering with the bioherms. F3

223   shows planar stratifications, low-angle to tabular cross-beddings, asymmetrical current ripples and

224   herringbone cross-beddings (Figs. 6A-B). The oolites are commonly spherical and concentric,

225   between 400 μm and 650 μm in diameter, associated with larger ones (asymmetric cortex) up to 2 mm.

226   Rosettes of sulphate minerals and bipyramidal quartz crystals are present within the oolites.

227   F3b includes aggregates (infra-mm to cm lumps and grapestones; Figs. 7D-F), intraclasts and oolites

228   floating in a microsparitic matrix. Intraclasts are elongated fragments of mudstones or microbial

229   laminites. Oolites are spherical to subspherical, asymmetric, micritic, and range from 500 μm to 1.5

230   mm in diameter.

231   F3c consists of homogeneous mudstones (Fig. 5D) or peloidal laminar wackestones to grainstones

232   (Fig. 5F) with peloids, oolites or proto-oolites. Angular, planar, cross-stratifications and herringbone

233   cross-beddings are common. The mudstone contains pyrite, pseudomorphs of sulphate minerals,

234   organic matter fragments, detrital quartz, feldspars, and micas. Replaced acicular rods and nodules of

235   sulphate (anhydrite relics) are present.

236   <u>Interpretation</u>

237   F3a likely formed between 1 to 6 m in water depth and more likely around 2 m-deep (Keith

238   and Zuppann, 1993) in high-energy shoals as attested by the occurrence of concentric oolites.

239   The shoals were later shortly exposed, as indicated by the presence of large asymmetric ooids

240   or vadoids (Beukes, 1983). Evaporite reflux or hypersaline conditions are shown by the

241   growth of sulphate crystals and bipyramidal quartz which are similar to those described by

242   Shukla and Friedman (1981) and by Mamet and Préat (2005). The sedimentary structures in

243   F3a point to waves and tidal currents reworking as attested by cross-beddings, herringbones

244   and asymmetrical ripples (Chakraborty, 2004; Boulvain, 2010).

245   F3b-c were deposited in low- to moderate-energy shallow waters located behind oolitic barrier

246   complexes (Bathurst, 1971) in the subtidal, intertidal and supratidal lagoonal environments,

247   locally disturbed by storms (Enos, 1983; Tucker et al., 1990). The sediments were submitted

248   to hypersaline conditions as shown by the pseudomorphs of evaporitic minerals.

249

250   *5.4. Facies association 4 (FA4)*

251   FA4 consists of pisoid floatstones (F3d), intraformational conglomerates (F4), laminar detrital

252   mudstones (F5) and stratiform stromatolites (F6).

253

254   <u>Description</u>

255   F3d consists of pisoid floatstones with asymmetric ooids (1.5 to 2 mm in diameter), peloids

256   and remains of microbial mats (Figs. 9A,D). The pisoids (2 mm to 5 cm in diameter) are

257   irregular, elongate or oval (Figs. 9B-C). Desiccation cracks, keystone vugs, pseudomorphs

258   after anhydrite (even in the pisoid nucleus) are common. Meniscus and pendular cementation

259   are observed, pointing to the presence of typical beach-rock. Intensive fragmentation formed a

260   breccia (F4).

261   F4 is a stratified conglomerate including micritic and centimetric intraclasts with rare 'ghosts'

262   of ooids giving a characteristic ''puzzle'' texture. Spiny and half moonlike oolites are

263   common. Desiccation cracks, calcitized laths or nodules of anhydrite and authigenic

264   bipyramidal quartz crystals are regularly observed.

265   F5 is laminar clayey detrital mudstones (Fig. 10) with detrital content up to 30% (dominant quartz and

266   feldspars) with alternations of light-colored laminae (silty fine sand to fine silt) and dark-colored

267   laminae (dominant pyrite). Desiccation-cracks and organic matter fragments are also associated.

268   F6 consists of gently wavy, flat-laminations with domal structures (Figs. 5E-F). Laminae consist of

269   alternation of darker organic-rich (with pyrite framboids) and lighter organic-poor layers. The matrix

270   contains dispersed idiotopic dolomite rhombs (up to 50 µm). The laminae are sometimes slightly

271   slumped and lenticular, deformed by crystallization of sulphate minerals occurring as microtepees.

272   Fenestral and crinkled fabrics, and near horizontal sheet-cracks associated with vertical mud-crack are

273   common.

274

275   <u>Interpretation</u>

276   FA4, including F3d to F6, represents peritidal environments submitted to periodic emersions.

277   F3d is indicative of vadose conditions on high-energy shoals with development of asymmetric

278   ooids, pendular and meniscus cements during emersion. This environment is similar to the

279   hypersaline supratidal zone in the Persian Gulf characterized by abundant pseudomorphs of

280   anhydrite (Scholle and Kinsman, 1974). F4 represents a low-energy shallow-water upper

281   intertidal to supratidal environments overprinted by episodic subaerial and marine-vadose

282   diagenesis. Such sediments were sporadically subject to evaporation in hypersaline conditions

283   as recorded by the precipitation of sulphates (Shearman, 1963; Kinsmann, 1969), spiny and

284   half-moon ooids (Flügel, 2004). Laminae associated with mud-cracks in F5 point to a low-

285   energy tidal flat environment in an upper intertidal to supratidal setting (Hardie, 1977;

286   Sellwood, 1986; Clough and Goldhammer, 2000). F6 is interpreted as evaporitic-dominated

287   low 'algal' marshes fringing ponds of channeled belts, similar with the Andros Island,

288   particularly along the backslope of the levees and the beach-ridge washovers (Hardie and

289   Ginsburg, 1977).

290

291   *5.5. Facies association 5 (FA5)*

292   <u>Description</u>

13

293 FA5 includes only clayey silty carbonates and dolomudstones (F7). It consists of stratified darkish

294 microparitized dolomicrite matrix with remnants of microbial mats (Figs. 11A-C). Slumping and

295 small-scale folding are observed. Sulphate (anhydrite, gypsum and polyhalite?) minerals are common

296 and consist of lath-shaped and rosette-like aggregates (Figs. 11D-E), enterolithic nodules, veins,

297 collapse breccias and castellated crystals (*sensu* Clark, 1980).

298

299 <u>Interpretation</u>

300 FA5points to an evaporitic peritidal environment (intertidal, temporarily emerged in the

301 supratidal zone), analogous to the recent littoral lagoons or sabkhas formed under warm semi-

302 arid conditions, along the Persian Gulf and the Mediterranean Coast (Patterson and Kinsman,

303 1981).

304

305 *5.6. Interpretation of depositional settings (Fig. 12)*

306 The SCI$_c$ Formation was deposited in a shallow ramp setting (*sensu* Burchette and Wright, 1992). It

307 exhibits clayey mudstones, microbial silty mudstones (outer-ramp), stromatolite biohermal, HCS

308 cross-bedded oolitic packstones/grainstones (mid-ramp) and vadose oolitic grainstones with

309 homogeneous wackestones and laminar microbial bindstones, capped by evaporate dolomudstones

310 (inner-ramp). The sediments were submitted to hypersaline conditions as shown by the abundant

311 pseudomorphs of evaporitic minerals.

312 The outer-ramp was a site of accumulation of terrigenous clay, silt and carbonate mud with microbial

313 MISS colonization in the quiet waters of the upper offshore at a depth of around 50 meters (FA1). The

314 most common mid-ramp facies are typical of shoreface transition environments with storm-wave

14

315   deposition of HCS oolitic series and giant stromatolites development with inter-reefal stromatoclast

316   accumulations (FA2). The inner-ramp facies are heterogeneous with high-energy environments in

317   oolitic sandy shoals, forming a nearshore variably effective barrier with lenticular units and low

318   energy environments in lagoonal settings behind the barrier. The inner-ramp facies are located above

319   the fair-weather wave base from the high-energy shoal and the low energy back-shoal (FA3) to inter-

320   and supratidal high energy beach proximal backshore environments with vadose cementation

321   (meniscus and pendant cements) and planar microbial mats (FA4) passing laterally to the sabkha

322   environments with hypersaline dolomudstones (FA5).

323

324   **6. Sequence Stratigraphy**

325   *6.1. Analysis of high-frequency cycles*

326   Sequence stratigraphy based on the recognition of sedimentary facies and unconformity surface

327   relationships have provided a predictive framework for the evolutionary history of the SCl$_c$ Formation.

328   The 27 sections (2 m to 57 m-thick) show the repetition of complete and incomplete cm to m-scale

329   sequences. The cyclicity is pervasive throughout the SCl$_c$ Formation and generally easy to identify in

330   the field. Five 'ideal' high-frequency shallowing-up cycles (5th order) are recognized in the SCl$_c$

331   Formation (Fig. 13 and Table 3); they are grouped in two main categories: (i) D-cycles (with D for

332   'deep') bounded by marine flooding surfaces, across which facies deepen and (ii) S-cycles (with S for

333   'shallow') bounded by subaerial exposures.

334   D cycles (2 m to 20 m-thick) are recognized from the lithological curve when a reset of F1 and/or F2

335   occurs while S cycles do not contain F1 and/or F2. The D cycles are homogeneous, displaying mainly

336   F1 and F2, their thicknesses are highly variable depending of the growth of the stromatolites up to 20

15

337   meters (F2). Evidence for major drowning unconformity in the SCI_c succession is provided by the clay

338   sedimentation associated with the MISS facies (see FA1, above) and by the development of giant

339   stromatolites initiating D1 and D2 cycles. The upper part of D-cycles is related to F6 with or without

340   typical products related to emersion or erosion.

341   S-cycles are centimetric-decimetric to 5-7 m-thick and show a shallowing-upward evolution, when

342   complete, near subaerial exposure conditions are recorded at their tops. They show evolution from an

343   oolite shoal to exposure surface associated with a sabkha environment: (i) the S1 cycle or 'oolite shoal

344   cycle' starts with F3a-b, (ii) the S2 cycle or 'lagoonal cycle' starts with F3c and (iii) the S3 cycle or

345   peritidal cycle starts with F3d. They contain several surfaces that can be erosive due to the scouring of

346   oolite shoals by currents, frequent in shallow-water carbonates (Tucker and Wright, 1990; Strasser,

347   2016). The S cycles are rather thinner and heterogeneous with a great variability in their facies

348   composition recording a shallow-water sedimentation sometimes with non-deposition in the supratidal

349   settings exhibiting numerous 'hiatal' surfaces. Their succession records high-frequency relative sea-

350   level changes in the upper part of the shallow shelf.

351   The stacking pattern of the shallowing-upward D and S m-scale cycles led to the recognition of

352   deepening and shallowing up parasequence sets (fourth-order, see below). Two typical sections (Saris

353   and D sections) are presented here as they allow following the successions of a few cycles (Figs. 14-

354   15; Table 4; Ackouala Mfere, 2017).

355   The parasequence sets (fourth-order) of both sections (and all others in Ackouala Mfere, 2017) are

356   aggradational and progradational.

357   The parasequence set package, deduced from the D and Saris section, is also recognized in many other

358   sections in the Niari-Comba subbasins of the NWCB from Zanzo at the East to Soulou at the West,

16

359   over more than 80 km (Fig. 3). As in Loutété (Sonocc quarry, Préat et al., 2018), it also consists of the

360   succession of the S1, S2 and S3 elementary cycles forming shallowing-upward packages.

361

362   *6.2. Sedimentary belts, Flooding (F) vs Forced Regression (FR) surfaces*

363   On the basis of the facies associations, we recognize at least three major successions which are partly,

364   or not entirely, superimposed as their precise succession cannot be specified due to the small thickness

365   of each of the studied sections (< 60 m, average ± 15-20 m). Each succession is characteristic of a part

366   of the ramp system and shows the succession of facies as follows (Fig. 16): ORS (outer-ramp

367   succession) with FA1, MRS (mid-ramp succession) with FA2, IRS (inner-ramp succession) with FA3-

368   4-5. Each succession is formed by the stacking of meter-scale shallowing-upward 5th-order or high-

369   frequency cycles (Ackouala Mfere, 2017). ORS succession (from W to E; example with sections O, F,

370   D) is generally thin-bedded and grades up into the massive stromatolitic bioherms of the MRS

371   succession (from W to E; sections T, N, P, F, K, H, B and MAD8019). MRS succession, comprising

372   the massive stromatolitic bioherms (e.g., from W to E; sections T, Q) shows oolitic units with HCS.

373   IRS succession consists of thin- to thick-bedded oolitic units (0.5 to 5 m thick) with trough, planar and

374   herringbone cross-laminations and homogeneous lagoonal units (from W to E, mainly in sections

375   MAD8016, O, M, F, H, D, B, MAS8018, MAD8019). Low-angle clinoforms are present suggesting

376   prograding washover oolitic deposits on the stromatolite bioherms (sections P and Q). The

377   interdigitation (not frequent) and the sharp (common) contacts observed in these two profiles between

378   the oolites and the massive bioherms indicate that the oolitic sands migrated partly during, and mainly

379   after, the biohermal growth.

17

380   Based on the different sections, IRS succession is the thickest (up to 55 m) and the ORS the thinnest.

381   The latter is probably thicker because, as being made of clays, it is easily weathered and thus good

382   outcrops are rare. The oolitic shoal has varying thicknesses of a few meters up to about a minimum of

383   30 m (section Q).

384   Lateral relationships between the three successions and their 4th and 5th order packages can be deduced

385   from sections T, N, P, Q?, F, K, H, D, B, MAD8019 as all these sections exhibit a marine flooding

386   surface, despite the packages they form, are not time constrained:

387   (i) most of the above mentioned profiles (F, K, H, D, B, MAD8019) have a similar stacking pattern

388   with alternation of meter-scale FA3/FA4. Lateral thickness variations cannot be established as the

389   sections are limited to the outcrop exposure, but it seems that for the thicker sections, the general

390   FA3/FA4 successions exhibit a similar thickness (~20-25 m) except in MAD8016 /MAD8018 with the

391   thickest thicknesses (at least twice or more if compared with the other sections). These alternations are

392   mostly composed of 5th order shallowing-upward S2 and S3-cycles with vadose diagenesis in the

393   pisoid grainstones (see sub-chapter 5.1), these cycles are grouped in 4th order parasequence sets

394   (Ackouala Mfere, 2017);

395   (ii) thick stacks (at least 30 m, section Q) of amalgamated packstone/grainstone shoal complexes

396   (FA3 *pro parte*) separating distally downdip biohermal stromatolites (FA2 *pro parte*). The dominantly

397   5th order progradational cycles (S1 cycles) are rather badly preserved due to the wedge-shaped cross-

398   beddings with planar and trough bedforms up to 1 m-thick and numerous inclined discontinuities

399   representing reactivation surfaces during storm-dominated processes (including HCS);

400   (iii) thin stacks (2-10 m-thick, sections T, F, D, B, MAD8018) of deeper facies assemblages (FA1 and

401   FA2 *pro parte*) with a few D aggradational cycles (subchapter 6.1).

402 In the different field sections, we recognized two types of erosional surfaces: marine flooding and

403 forced regression surfaces. Marine flooding surfaces ('F' surfaces) are characterized by a sharp

404 deepening upward in the depositional environments from inner to outer ramp deposits (from W to E;

405 sections T, N, P, Q?, F, D, B, MAD8019, in this latter section three repeated flooding surfaces are

406 present; Fig. 16). One of them, being the only continuous surface, correlates laterally over long

407 distances, is interpreted as a transgressive surface (TS surface). Forced regression surface (FR surface)

408 is also recognized in most places. It is marked by an abrupt passage from offshore facies of the outer

409 ramp (FA1) to the shallow-water inner-ramp facies (FA4) (from W to E; sections O and F) with no

410 evidence of extensive subaerial exposure. In most places, the FR surface underlines prograding oolitic

411 shoal deposits. This surface originates from a falling stage of the base level from the offshore to the

412 proximal backshore, which in our succession represents a sea-level fall of a few tens of meters as

413 facies FA1 ($\pm$ 40-50m deep) is directly covered by facies FA4 (0-10 m deep).

414 From the detailed analysis of the 27 sections, we propose an 'ideal' or 'virtual' synthetic SCI

415 succession. It starts with section MAD8019 (with three flooding surfaces), overlain by section Q with

416 the thickest oolite shoal above a FR surface (Fig. 16) and covered by section MAD8018 (with the

417 thickest peritidal facies and silty evaporites at the SCII boundary). The oolite shoals and reefal bodies

418 are parallel and accumulated along a W-E 100 km-long regional axis bordering the Archean Congo

419 Craton located in the North. Based on the recently revised geological map and personal information of

420 BRGM (pers. communication, Y. Callec, BRGM) the width of the oolite shoal is about 30-60 km.

421

422 **7. Discussion**

423 *7.1. Distribution of stromatolites in the Niari-Nyanga and Comba subbasins of the NWCB*

19

424   Giant stromatolitic bioherms are more developed in the eastern part of the studied area while

425   they are rare and thin (less than 1 m) in the western part (Fig. 16) reflecting probably the

426   variation of the accommodation space.

427   Growth of the main reef builders is affected by a multitude of environmental factors, such as

428   temperature, illumination, turbidity, substrate, and nutrients levels. Many of these factors vary

429   systematically with depth, and this has led to recognition of reefal depth-related zonations in

430   the Phanerozoic rocks (James and Bourque, 1992), and in the early Neoproterozoic series

431   (Bertrand-Sarfati and Moussine-Pouchkine, 1985; Sarkar and Bose, 1992). Alvarez and

432   Maurin (1991) described a NE deepening of the basin with the development of giant

433   stromatolitic bioherms located at the "junction" between the Niari-Nyanga and Comba

434   subbasins of the NWCB (Bertrand-Sarfati and Vicat, 1987; Trompette and Boudzoumou,

435   1988). Variation of the accommodation space has controlled the shape and the vertical

436   development of the reefs in the SCI_c Formation. Giant stromatolitic bioherms grew during a

437   relative high sea-level where light and oxygen were sufficient to promote the activity of

438   cyanobacteria as shown previously with the stacks of bodies up to 20 m in height. On the

439   contrary, the flat and laminar stromatolites with small domes (< 80 cm) recorded a

440   progradational phase, most likely because limited accommodation space did not permit

441   development of giant stromatolites.

442

443   *7.2. Evidence of storm events in the carbonates of the SCI_c Formation*

444   The oolitic grainstones-packstones show undulating bedding referred to as HCS (Dott and Bourgeois,

445   1982; Duke, 1985; Morsilli and Pomar, 2012), indicative of storm events in the shoreface transition as

20

446 the greatest potential preservation of these structures is between the fair weather- and storm-wave

447 bases, that is a few to several tens of meters (Dott and Bourgeois, 1982; Dumas and Arnott, 2006).

448 These high-energy conditions bring a large amount of sediment into suspension near the sea floor and

449 the mixture of sediment and water oscillates back and forth from shallow to deep waters. Although

450 most oolites form in wave-dominated shallow water shoals (commonly about 2 m), these grains are

451 readily dispersed by storm return currents in deeper water settings.

452 The general successions exposed in the oolite shoals usually reveal an upward transition from HCS to

453 low-angle tabular cross-bedding. This transition reflects an increase in water hydrodynamics and a

454 shallowing up trend from shoreface to beachface environments. Prograding sequences have been

455 documented in many successions with storm effects indicating an upward decrease in water depth

456 (Dott et Bourgeois, 1982), as in an Indian Neoproterozoic ramp (Chakraborty, 2004) and in the

457 Neoproterozoic Bambuí basin of central-eastern Brazil, which lays on top of the same craton with the

458 West Congo units on the other slide of the Atlantic (Uhlein et al., 2019).

459 In the SCI$_c$ Formation, high-energy events are also attested by the elongated stromaclasts (up

460 to 5 cm in length) accumulated in inter-reef areas between the stromatolites. These high-

461 energy events were probably related to episodic storms that formed the HCS in the oolite

462 shoals.

463

464 *7.3. Development of systems tracts*

465 In the absence of time constraints on sequence stratigraphy hierarchy, the key physical

466 bounding surfaces (flooding and forced regression) and the stacking pattern analysis of high

467 frequency cycles (S *vs*. D) help in deciphering the stratigraphic pattern in the basin. The SCI

21

468 is interpreted as a single third-order transgressive-regressive sequence which includes a

469 transgressive systems tract (TST) and a highstand systems tract (HST) after the post-Marinoan

470 deglaciation event (Alvarez, 1995). We here interpret the SCI Subgroup as two transgressive-

471 regressive third-order sequences (Fig. 17). In the first sequence, TST sedimentation started

472 with deposition of the 10-12 m-thick cap carbonates (SCI_a) and about 10-15 m-thick of

473 siliciclastic deposits (lower SCI_b). This latter is followed by an HST phase (upper SCI_b, about

474 135 m-thick) above a maximum flooding surface (MFS). In the second sequence starting with

475 the SCI_c, a lowstand systems tract (LST) is initiated with very shallow water deposits

476 characterized by the alternation of FA3/FA4 with abundant S2 cycles. The LST is overlain by

477 a TS leading to the development of the 'deep' MISS facies (TST). The MFS above the TST is

478 followed by a HST (giant stromatolites). Favorable environmental conditions helped by high

479 accommodation rates after deposition of mud and siliciclastic layers (MISS facies in our case)

480 resulted in growth of giant stromatolites as described in the Proterozoic ramp of Australia

481 (Sami et al., 2000). Stromatolite growth was surely unable to keep pace with initial sea-level

482 rise, resulting in the deposition of mud-dominated sediments (MISS facies), which probably

483 represents a "condensed" interval.

484 The HST is marked by complete or incomplete aggradational shallowing-upward cycles as

485 shown in Zanzo, B, D, H, K and F sections (Fig. 16). Laterally, the giant stromatolites

486 interfinger with hummocky cross-bedded oolitic grainstones.

487 In most places, the giant stromatolites are sharply buried by trough cross-bedded oolitic

488 grainstones (S1 cycles) in a forced regression systems tract (FRST) evolving to subtidal and

489 peritidal facies near emersion (S2 and S3 cycles), when reduced accommodation rates

22

490   facilitated the accumulation of the shallowest facies. In some sections, interdigitation with

491   lateral pinch-outs between the giant columnar stromatolites (F2) and the oolite shoals (F3) has

492   been observed. They can be followed laterally over a minimum of a few meters, depending on

493   the size of the outcrops. This interdigitation represents a lateral facies change from giant

494   columnar stromatolites to oolite shoals, which also overlay the stromatolites. Thick oolite

495   shoal stacking units, above the FR surface (see sections T, Q) shows that progradation

496   accelerated with time during the FRST probably due to a net fall of sea-level. Sea-level fall

497   could also be recorded in section Q with exposed areas of carbonate sediments, which

498   produced oolite dunes or large-sized lenses (sections Q and R) as a result of tidal processes.

499   At the transition to SCII, the succession is marked by deposition of silty evaporites and

500   dolomites at the top of MAD8018 section (Fig. 16). These silty evaporites and dolomites

501   represent a LST of the next sequence in the SCII series. (Fig. 17).

502

503   *7.4. Facies correlations between the Niari-Nyanga and Comba subbasins in RC to the Lower Congo*

504   *subbasins in DRC*

505   The C3 Formation (SCI$_c$ equivalent in Lower Congo, DRC) about 240 m-thick, dominantly contains

506   light-grey limestones with greenish-grey shales (C3a Member), and massive to crossed-bedded light

507   grey to whitish oolitic and pisoid limestones with thin layers of greenish shales and intraformational

508   conglomerates (C3b Member) (Lepersonne, 1974; Cailteux et al., 2015; Delpomdor et al., 2015,

509   2019). The standard sequence starts with open marine environments and oolitic shoals passing to

510   restricted peritidal/sabhka environments behind the oolite shoals in a mid- to inner-ramp setting

511   (Delpomdor et al., 2015, 2019). Due to the long distance (around 150 km between the sections in RC

23

512   and DRC) and the absence of globally-correlative marker levels in these unfossiliferous series, the

513   current correlation of SCI$_b$ and SCI$_c$ with respectively C2 and C3 series is a quite simplistic useful

514   interpretation; see Fig. 17. For example, the lowermost part of the SCI$_b$ series consisting of marls and

515   marly limestones, locally limestones in the loop of the Niari river (Dadet, 1969), could be coeval with

516   the lowermost part of the C2 Formation (e.g., C2a to C2c members; stratigraphic correlation after

517   Cahen, 1978), while the uppermost part of the C2 Formation (e.g., C2d to C2e members) consisting of

518   calcareous shales, sandy and muddy limestones and limestones (Delhaye and Sluys, 1923;

519   Lepersonne, 1974; Cailteux et al., 2015; Delpomdor et al., 2015) could be coeval with the upper part

520   of the SCI$_b$ Formation, which is mainly constituted of marly limestones and limestones (Dadet, 1969).

521   The lowermost member of the SCI$_c$ series (e.g., SCI$_{c-a}$ Member) could be laterally coeval with the C2f

522   to C2g members of the C2 Formation, which consist of calcareous shales, sandstones and limestones.

523   The C3 Formation, divided into C3a and C3b members (Cailteux et al., 2015) is proposed in this study

524   as coeval with the lower and upper part of the SCI$_c$ series respectively. Correlation from these

525   shallow-water series with multiple shoaling events deduced from the lithologic patterns is therefore

526   difficult and could be improved by using the sequence stratigraphy data of our work in RC and the

527   study of Delpomdor et al. (2015) in DRC. These marine deposits formed in extensive near shore

528   environments during a global transgression related to the probable deglaciation at the end of Snowball

529   Earth. In both areas, the shelf was block-faulted and structured into highs and shallow depressions,

530   creating complex morphologies as suggested by Alvarez and Maurin (1991) in the Niari-Comba area.

531   Our detailed stratigraphic sequence analysis of the Comba aulacogen combined with paleobathymetric

532   data allows correlation of third-order sequence between the two areas (RC and RDC) (Fig. 17). This

533   reveals that the SCI$_b$ is partly related to a TST phase (SCI$_a$ and lower SCI$_b$ in RC or C2a-b members in

24

534 DRC) and an HST phase (upper SCI$_b$ in RC or C2c-e members in DRC). The extreme uppermost part

535 of the C2 formation, e.g., C2f to Ce2h members; observation by Sikorski, 1958) in DRC could

536 laterally correspond to facies recording a LST in RC, and the C3a Member to TST and HST recorded

537 in the lowermost part of the SCI$_c$ series in RC, if we consider that the giant stromatolites never

538 described in DRC are included in this formation. After the lowstand to highstand sequence, the oolite

539 shoals (C3b Member) or the uppermost part of the SCI$_c$ is newly reinterpreted as FRST marked by the

540 progradation of oolite shoals evolving to peritidal facies near emersion atop of the SCI$_c$ series and C3

541 Formation, when reduced accommodation rates facilitated the accumulation of shallowest facies. As

542 suggested by Delpomdor et al. (2015), the top of the C3 Formation has been exposed to erosion/and or

543 karstification suggesting a regional-scale turn off the carbonate factory. In this context, the silty

544 evaporates at the transition SCI-SCII are interpreted as a LST in the next sequence (SCII Formation in

545 RC or C4 in DRC).

546 However, we interpret the three positive jumps of the Fischer plot present in the C3a2 to C3b2 units

547 (Delpomdor et al., 2015) as probably related to reactivations of the block-faulting observed in the SCI$_c$

548 Formation, in this case related by flooding surfaces (Fig. 16). Both areas experienced basin tectonics

549 in the general context of a pre-collisional phase creating changes in relative sea-level by reactivation

550 of pre-existing faults. This implies that the parasequence packages are strongly controlled by tectonics

551 and are diachronous on the scale of the whole basin. Our sequence stratigraphic analysis allows for the

552 first time tentative correlation in the Schisto-Calcaire Group and Lukala Subgroup in RC and DRC

553 respectively. Giant stromatolites observed in RC were identified in the lowermost part of the SCIc

554 series, while stromatolitic reefs (10 m long and a few meters width), associated with breccias and

555 oolitic limestones have been found in the C3b Member (Cahen, 1950). Recently, microbial mats have

25

556   been identified in the C3a Member in DRC (Delpomdor et al., 2015). As shown previously, water

557   depth is the first-order control on reef growth and morphology. Deep water is essential for

558   development of giant stromatolites but cyanobacteria need also fine grained sand substrate for best

559   development, as shown previously with the MISS of the F1 (Noffke, 2010). Giant domal stromatolites

560   commonly form in deep water settings (Bertrand-Sarfati and Moussine-Pouchkine, 1985; Dill et al.,

561   1986; Glumac and Walker, 2000) while flat morphologies occur in shallow water settings (Arenas and

562   Pomar, 2010; Glumac and Walker, 2000). Water depth was probably higher in the sedimentary areas

563   located in RC than in the DRC as a result of the structuration of this area by tectonic effects during

564   sedimentation. Although the geometry of deposits of the SCI$_c$ Formation is seen as continuous on the

565   southern edge of the Chaillu Massif, Chorowitz et al. (1990) concluded that the Lower Congo/Sangha

566   aulacogen, extended to the Comba aulacogen, shows multiple pull-apart-type tectonic areas

567   constituted of elongated WNW-ESE tilted blocks defined by NE-SW faults. Therefore, the

568   sedimentation records the development of oolite shoals. The development of a cordon of oolitic sands

569   of the C3 Formation in DRC, similar to the SCI$_c$ Formation of RC, may also be inferred on the NW

570   edge of the Kasaï block. The oolitic shoals seem to bypass the NW Kasaï block by the thickening of

571   oolitic limestones (100-200 m in thickness) in Angola (Schermerhorn and Stanton, 1963).

572

573   *7.5. Origin of cyclicity*

574   Facies analysis led to the recognition of a cyclic pattern in the SCI$_c$ sedimentation. Generally, the

575   recognized cycles exhibit a shallowing-upward trend, as suggested by the vertical facies evolution

576   along the standard sequence. Autocyclic and allocyclic mechanisms can both lead to shallowing-

577   upward cycles (Strasser, 1991). While autocyclic processes operate within the sedimentary basin with

578   progradation of tidal flat or lateral migration of tidal channels (Satterley, 1996), allocyclic control

579   mechanisms are independent of the depositional processes and include eustatic sea-level fluctuations

580   (Elrick, 1995) or repeated synsedimentary tectonic downfaulting events, e.g., tectonics model

581   proposed by Cisne (1986). Subsidence does not appear to have been constant during deposition of

582   SCI_c Formation over the whole studied area as the SCI_c thicknesses show important variations; rather

583   it was affected by periodic changes. On the other hand, SCI_c cyclic deposition (fourth-order) is not

584   harmonious, and the cycles are difficult to correlate between neighboring sections (less than a few

585   kilometers) despite the overall regressive depositional trend of the stratigraphic interval and the

586   consistent shallowing-upward parasequence trend within the sections.

587   There are a variable number of elementary parasequences (fifth-order) at each locality suggesting that

588   most are probably the result of migration of local environments due to multiple shoaling events. In this

589   context, these parasequences seem to be autocyclic (Ginsburg, 1971) and represent the typical

590   evolution (migration, erosion, non deposition) of ooid dunes controlled by currents and sea-level

591   fluctuations at very shallow depths. Moreover, accumulation rate variations and diagenesis could also

592   modified the final shapes of the SCI_c stratigraphical data sets. Additionally, several subaerial

593   exposures of the investigated sections and erosional boundaries suggest periodical drops of the relative

594   sea-level followed by renewed transgressions.

595   Assuming that the autocyclic mechanism originated from aggradational/progradational trends during

596   deposition of the SCI_c Formation, this process suggests a particular factor affecting the Niari-Nyanga

597   and Comba subbasins of the NWCB to drive the changes in the accommodation space. A tectonic

598   control with reactivation of pre-existing faults (leading to multiple episodes of accommodation space

599   changes) may play a role in the origin of these cycles (see below, 6.6.)

600   The fact that D1 cycles are directly overlain by progradational facies suggests that there was no true

601   drowning and they were not associated with a true eustatic sea-level increase. They have been related

602   to local interference by tectonic movement or autocyclic processes. The lateral and vertical

603   variabilities of thickness of the elementary parasequences could be attributed not only to the variable

604   potential of sediment accumulation in the different environments (shoal, back-shoal, tidal channels,

605   lagoon, shoreface) but also to the tectonic context that created the Niari-Comba subbasins of the

606   NWCB. As a result, random processes dominated and blurred the low-amplitude sea-level signal, and

607   the resulting sedimentary records will differ depending on their location in the basin (Strasser, 2016).

608   The sedimentary environments were generally shallow enough to record the several relative sea-level

609   fluctuations (1-5 m) and produced the common observed S-cycles. As no order or regularity in the

610   cycle pattern is observed, as could be expected if orbital forcing was the dominant mechanism, it is

611   highly probable that autocyclic processes (helped or inferred by tectonics) were dominant, in a general

612   tectonic setting with both constant and differential subsidence along various faulted blocks.

613

614   *7.6. Tectonic significance and regional implication*

615   All of the high-order cycles identified in the SCI$_c$ Formation were deposited under conditions of sea-

616   level fluctuations driven by tectono-eustasy, which dominated the late Neoproterozoic.

617   During Neoproterozoic times, several distinct extensional tectonic episodes affected the São

618   Francisco-Congo Craton in the area related to the development of the AWCO (Pedrosa-Soares and

619   Alkmin, 2011). After 660 Ma, a passive margin developed in the WCB with deposition of the

620   Bouenza-Louila Subgroup in RC, the stratigraphic equivalent Haut-Shiloango Subgroup in DRC,

621   followed by respectively the Upper Diamictite Formation and the Lukala Subgroup (Frimmel et al.,

622   2006; Poidevin, 2007). These movements in the basin reflected pre-Marinoan extensional events (see

623   Pedrosa-Soares and Alkmin, 2011), enhancing tectono-eustatic fluctuations during the pre-, syn- and

624   post-sedimentary deposition (Delpomdor et al., 2015, 2016, 2019). Under these passive margin

625   conditions, the relative eustatic variations in the SCI_c Formation are the consequence of short-time

626   extensional tectonic activities in the whole basin including several sub-events in Central Africa and

627   recorded through the fifth-order D- and S-cycles. Deepening occurred when relative sea-level and/or

628   accommodation space increased due to short-time extensional tectonic activities leading to the

629   drowning of the former inner-ramp areas.

630   The same cyclicities have been recognized in the C3 Formation in Lower Congo (Delpomdor et al.,

631   2015, 2019). The tectonics was probably related to the breakup of Rodinia which influenced

632   sedimentary processes through tectonic subsidence and sediment supply in a similar way as occurred

633   along opposing paleo-Atlantic and paleo-Pacific margins of Laurentia (Eyles and Januszczak, 2004).

634   Even if the timing of the series is poorly constrained in order to establish detailed correlations between

635   the lower part of the Schisto-Calcaire Group in SW Gabon (Préat et al., 2010), Lower Congo region

636   (Delpomdor and Préat, 2013) and our studied area, it appears that the SCI_c overlying the reddish

637   calcareous marls and marls (SCI_b Formation) is coeval with the Nsc1c (Préat et al., 2011, 2018), and

638   probably the top of the C2 Formation and with the C3 Formation in Lower Congo region (DRC;

639   Delpomdor et al., 2015). As shown by Delpomdor et al. (2015, 2019) and in our study, this

640   sedimentation exposes mainly shallowing-upward cycles in response to tectono-eustasy occurring in

641   the late Neoproterozoic (Tack et al., 2001; Li et al., 2008; Delpomdor and Préat, 2013). In RC, general

642   sea-level rise did not occur in one continuous phase as highlighted by the recurrence of the D1 cycles

643   in (D, H, Zanzo, F and T sections; Fig. 16), but was probably triggered by the reactivation of regional

29

644 block-faulting (see Strasser, 2016 for general consideration) with extensional faults related to the

645 rifting evolution of the Comba aulacogen (see above). The lateral variability in the thickness of the

646 elementary parasequences (Ackouala Mfere, 2017) is therefore attributed not only to the variable

647 potential of sediment accumulation in the different environments but also to synsedimentary tectonics.

648

649 **8. Conclusions**

650 The SCI_c Formation was formed in a paleoramp setting from quiet water in the outer-ramp (FA1) to

651 very shallow water under hypersaline conditions in the inner-ramp (FA5). Storm events have been

652 recognized by HCS in the oolitic series and by elongate stromaclasts (up to 5 cm in length)

653 accumulated in inter-reef areas between the stromatolitic bioherms (FA2). The SCI_c Formation records

654 LST, TST, HST and FRST successions (Fig. 17) linked to the reactivation of regional block-faulting

655 and is also marked by a regional TS (Fig. 16). The D and S-cycles or elementary parasequences

656 (meter-scale from 0.1 to 20 meters in thickness) are well developed in the carbonate ramp from outer-

657 to inner-settings with dominant S1 cycles in high energy settings and lagoonal S2 cycles in low energy

658 settings. The magnitude of the sea-level change was mostly small (except during the transgression and

659 the forced regression), less than a few meters as deduced from the average of the tidal cycle ticknesses

660 (1-3 m-thick). This produced a random stack of elementary parasequences, as for example where

661 shoals migrated out of main transport path. The LST in the SCI_c Formation is represented by the

662 maximum of progradation of the whole SCI Subgroup, with decreasing circulation and fluctuating

663 salinities, reflected by development of a sabkha environment with dolomudstones and abundant

664 sulphate pseudomorphs (FA5), also pointing to a probable climate change from semi-arid to arid

665 setting. The SCI_c Formation records high-frequency shallowing-upward cycles generated by an

666 autocyclic mechanism that is likely controlled by tectonic syn-sedimentary extensional faults related

667 to the rifting of the basin. On a broader scale, the recurrent generation of accommodation space was

668 triggered by short-time extensional tectonic activity related to several sub-events in Central Africa.

669 The cyclic succession of the fourth-order parasequences in the SCI$_c$ Formation has been correlated

670 between the studied sections following the general trend. In detail, each section shows a specific

671 evolution, as for example the FR observed in two sections. The stratigraphic package of the SCI$_c$

672 Formation can be subdivided into two broad 4th-order sequential units: the first one comprises

673 packages of the laminar clayey silty mudstones (MISS facies) and stromatolite bioherms, the second

674 starts with ooid shoals and is terminated by evaporative dolomudstones. This 'binome' formed of

675 packages of elementary parasequences can be traced across the whole shelf, even while it is

676 impossible to trace the individual parasequences and occurs over more than 100 km reflecting the

677 sedimentary filling of the basin, which is probably tectonically driven. The elementary parasequences

678 and their grouping are diachronic, they do not produce a clear stacking pattern, and cannot be used for

679 chronostratigraphy. Their distribution is related to the amount of accommodation space available,

680 which is primarily controlled by differential subsidence among the faulted-blocks. The best correlation

681 across the basin (from Gabon to Angola) is surely the recognition of this 'binome'.

682

688 and the editor Damien Delvaux for their constructive reviews and helpful criticism.

689

690 **Bibliography**

691 Ackouala Mfere, A.P., 2017. Sédimentologie, Cyclicité et Diagenèse des Carbonates de la Formation

692   du Schisto-Calcaire (SCIc) dans les sous-bassins de Niari-Nyanga et de Comba en République

693   du Congo, PhD thesis, Université Libre de Bruxelles, 265pp.

694 Affaton, P., Kalsbeek, F., Boudzoumou, F., Trompette, R., Thrane, K., Frei, R., 2016. The Pan-

695   African West Congo belt in the Republic of Congo (Congo Brazzaville): Stratigraphy of the

696   Mayombe and West Congo Supergroups studied by detrital zircon geochronology. Precambrian

697   Res. 272, 185–202. https://doi.org/10.1016/J.PRECAMRES.2015.10.020

698

699 Allen, P.A., Leather, J., Brasier, M.D., 2004. The Neoproterozoic Fiq glaciation and its aftermath,

700   Huqf supergroup of Oman. Basin Res. 16, 507–534. https://doi.org/10.1111/j.1365-

701   2117.2004.00249.x

702

703 Alvarez, P., Maurin, J.-C., 1991. Evolution sédimentaire et tectonique du bassin protérozoïque

704   supérieur de Comba (Congo) : Stratigraphie séquentielle du Supergroupe Ouest-Congolien et

705   modèle d'amortissement sur décrochements dans le contexte de la tectogénèse panafricaine.

706   Precambrian Res. 50, 137–171. https://doi.org/10.1016/0301-9268(91)90051-B

707

708 Alvarez, P., 1995. Evidence for a Neoproterozoic carbonate ramp on the northern edge of the Central
709 African craton: relations with Late Proterozoic intracratonic troughs. Geol. Rundsch. 84, 636-648.
710
711 Arenas, C., Pomar, L., 2010. Microbial deposits in upper Miocene carbonates, Mallorca, Spain.

712   Palaeogeogr. Palaeoclimatol. Palaeoecol. 297, 465–485.

713   https://doi.org/10.1016/J.PALAEO.2010.08.030

714 Arnaud, E., Eyles, C.H., 2006. Neoproterozoic environmental change recorded in the Port Askaig

715   Formation, Scotland: Climatic vs tectonic controls. Sediment. Geol. 183, 99–124.

716   https://doi.org/10.1016/J.SEDGEO.2005.09.014

717 Bathurst, R.G.C., 1971. Carbonate sediments and their diagenesis, Elsevier, Amsterdam.

718   https://doi.org/10.1016/0016-7185(73)90072-9

719 Baudet, D., Fernandez, M., Kant-Kabalu, F. & Laghmouch, M., 2013. Carte géologique de la

720   République Démocratique du Congo au 1/500 000- Province du Bas-Congo. Musée royal de

721   l'Afrique centrale, Tervuren, Belgique & Centre de Recherches Géologiques et Minières,

722   Kinshasa, RD Congo, avec une notice explicative de 50p.

723   Bertrand-Sarfati, J., Moussine-Pouchkine, A., 1985. Evolution and environmental conditions of

724   Conophyton-Jacutophyton associations in the Atar dolomite (Upper Proterozoic, Mauritania).

725   Precambrian Res. 29, 207–234. https://doi.org/10.1016/0301-9268(85)90069-5

726   Bertrand-Sarfati, J., Vicat, J.P., 1987. Les stromatolites columnaires du Schisto-Calcaire du

727   Protérozoïque Supérieur du Congo et leur place dans la sédimentation. Bull. Société Géologique

728   Fr. III, 289–298. https://doi.org/10.2113/gssgfbull.iii.2.289

729   Beukes, N.J., 1983. Ooids and oolites of the proterophytic Boomplaas Formation, Transvaal

730   Supergroup, Griqualand West, South Africa, Coated grains. Springer Berlin Heidelberg, Berlin,

731   Heidelberg. https://doi.org/10.1007/978-3-642-68869-0_18

732   Bose, P.K., Chaudhuri, A.K., 1990. Tide versus storm in epeiric coastal deposition: Two Proterozoic

733   sequences, India. Geol. J. 25, 81–101. https://doi.org/10.1002/gj.3350250203

734   Boulvain, F., 2010. Pétrologie sédimentaire des roches aux processus. Ellipses.

735   Burchette, T.P., Wright, V.P., 1992. Carbonate ramp depositional systems. Sediment. Geol. 79, 3–57.

736   Cahen, L., 1950. Le Calcaire de Sekelolo, le Complexe tillitique et la Dolomie rose C1 dans

737   l'Anticlinal de Congo dia Kati (Bas-Congo). Annales du Musée royal du Congo belge, Tervuren,

738   in 8°. Sciences Géologique. 7, 55 pp.

739   Cahen, L., 1978. La stratigraphie et la tectonique du Super- Nd isotope ratios are listed in Table 5.

740   Ages were groupe Ouest-Congolien dans les zones me ´diane et externe calculated following

741   Ludwig (1999). de l'orogène Ouest-Congolien (Pan-Africain) au Bas-Zaïre et dans les régions

742   voisines. Ann. Mus. R. Afr. Centr., 3 Tervuren (Belg.), in-8°, Sci. Géol. 83, p.150

743   Carto, S.L., Eyles, N., 2012. Sedimentology of the Neoproterozoic (c. 580 Ma) Squantum "Tillite",

744   Boston Basin, USA: Mass flow deposition in a deep-water arc basin lacking direct glacial

745   influence. Sediment. Geol. 269–270, 1–14. https://doi.org/10.1016/J.SEDGEO.2012.03.011

746   Chakraborty, P.P., 2004. Facies architecture and sequence development in a Neoproterozoic carbonate

747   ramp: Lakheri Limestone Member, Vindhyan Supergroup, Central India. Precambrian Res. 132,

748   29–53. https://doi.org/10.1016/J.PRECAMRES.2004.02.004

749   Charles, N., Callec, Y., Préat, A., Thiéblemont, D., Delpomdor, F., Malounguila, D., Gloanguen, E.,

750   Petitot, J., Ackouala, A.-P., Ndiele, B., Mvoula boungou, I., Moebo Boungou, M., 2015. Notice

751   explicative de la carte géologique de la République du Congo à 1/200 000, Feuille Madingou.

752   Editions BRGM, 225 pp.

753   Cailteux, J.L.H., Delpomdor, F.R.A., Ngoie Ndobani, J.-P., 2015. The Neoproterozoic West-Congo

754   "Schisto-Calcaire" sedimentary succession from the Bas-Congo region (Democratic Republic of the

755   Congo) in the frame of regional tentative correlations. Geol. Belg. 18, 126-146.

756

757   Clark, D.., 1980. The diagenesis of Zechstein carbonate sediments. In: Füchtbauer, H., Peryt, T.

758   (Eds.), The Zechstein Basin with Emphasis on Carbonate Sequences. Stuttgart, E.

759   Schweizerbart'sche Verlagbuchandlung. Contrib. to Sedimentol. 9, 16.

760

761   Chorowitz, J., Le Fournier, J., Mvumbi, M.., 1990. La Cuvette Centrale du Zaïre: un bassin initié au

762   Protérozoïque supérieur. Contribution de l'analyse du réseau hydrographique. Comptes-Rendus

763   l'Académie des Sci. Paris 331, 349–356.

764   Cisne, J.L., 1986. Earthquakes recorded stratigraphically on carbonate platforms. Nature 323, 320–

765   322. https://doi.org/10.1038/323320a0

766   Clough, J.G., Goldhammer, R.K., 2000. Evolution of the Neoproterozoic dolomite ramp complex,

767   Northeastern Brooks range, Alaska. In: Grotzinger, J.P., James, N.P. (Eds.). Carbonate

768   sedimentation and diagenesis in the evolving Precambrian world. Soc. Econ. Paleontol. Mineral.

769   Spec. Publ. 209–241.

770

771   Dadet, P., 1969. Notice explicative de la carte géologique de la République du Congo Brazzaville au

772   1/500000. Mémoire du Bureau de Recherches Géologiques et Minières 40, 103.

773   Delhaye, F., Sluys,M., 1923. Esquisse géologique du Congo occidentale. Etude du système Schisto-

774   Calcaire, missions géologiques de 1914 et 1918–19. Etablissement Cartographique E. Patesson,

775   Bruxelles-Uccle, 1923–1924.

776   De Paepe, P., Hertogen, J., Tack, L., 1975. Mise en évidence de laves en coussins dans les faciès

777   volcaniques basiques du massif de Kimbungu (Bas-Zaïre) et implications pour le magmatisme

778   Ouest-Congolien 98, 251–270.

779 Delpomdor, F., Eyles, N., Tack, L., Préat, A., 2016. Pre- and post-Marinoan carbonate facies of the

780   Democratic Republic of the Congo: Glacially- or tectonically-influenced deep-water sediments?

781   Palaeogeogr. Palaeoclimatol. Palaeoecol. 457, 144–157.

782   https://doi.org/10.1016/J.PALAEO.2016.06.014

783 Delpomdor, F., Tack, L., Cailteux, J., Préat, A., 2015. The C2 and C3 formations of the Schisto-

784 Calcaire Group (West Congolian Supergroup) in the Democratic Republic of the Congo: an example

785 of Post-Marinoan sea level fluctuations as a result of extensional tectonisms. J. Afr. Earth Sci. 110, 14-

786 33.

787

788 Delpomdor, F., Préat, A., 2013a. Early and late neoproterozoic c, o and sr isotope chemostratigraphy

789   in the carbonates of west congo and mbuji-mayi supergroups: A preserved marine signature?

790   Palaeogeogr. Palaeoclimatol. Palaeoecol. 389, 35–47.

791   https://doi.org/10.1016/j.palaeo.2013.07.007

792 Delpomdor, F., Préat, A., 2013b. Early and late Neoproterozoic C, O and Sr isotope

793   chemostratigraphy in the carbonates of West Congo and Mbuji-Mayi supergroups: A preserved

794   marine signature? Palaeogeogr. Palaeoclimatol. Palaeoecol. 389, 35–47.

795   https://doi.org/10.1016/J.PALAEO.2013.07.007

796 Delpomdor, F., Van Vliet, N., Devleeschouwer, X., Tack, L., Préat, A., 2018. Evolution and estimated

797   age of the C5 Lukala carbonate-evaporite ramp complex in the Lower Congo region (Democratic

798   Republic of Congo): New perspectives in Central Africa. J. African Earth Sci. 137, 261–277.

799   https://doi.org/10.1016/J.JAFREARSCI.2017.10.021

800 Delpomdor, R.A., 2017. Facies and micromorphology of the Neoproterozoic Upper Diamictite

801   Formation in the Democratic Republic of Congo : new evidence of sediment gravity flow.

802

803 Deynoux, M., Affaton, P., Trompette, R., Villeneuve, M., 2006. Pan-African tectonic evolution and

804   glacial events registered in Neoproterozoic to Cambrian cratonic and foreland basins ofWest

805   Africa. J. Afr. Earth Sci. 46, 397–426.

806 Dill, R.F., Shinn, E.A., Jones, A.T., Kelly, K., Steinen, R.P., 1986. Giant subtidal stromatolites

35

807   forming in normal salinity waters. Nature 324, 55–58. https://doi.org/10.1038/324055a0

808   Direen, N.G., Jago, J.B., 2008. The Cottons Breccia (Ediacaran) and its tectonostratigraphic context

809   within the Grassy Group, King Island, Australia: A rift-related gravity slump deposit.

810   Precambrian Res. 165, 1–14. https://doi.org/10.1016/J.PRECAMRES.2008.05.008

811   Dott, R.H., Bourgeois, J., 1982. Hummocky stratification: Significance of its variable bedding

812   sequences. Geol. Soc. Am. Bull. 93, 663. https://doi.org/10.1130/0016-

813   7606(1982)93<663:HSSOIV>2.0.CO;2

814   Duke, W.L., 1985. Hummocky cross-stratification, tropical hurricanes, and intense winter storms.

815   Sedimentology 32, 167–194. https://doi.org/10.1111/j.1365-3091.1985.tb00502.x

816   Dumas, S., Arnott, R.W.C., 2006. Origin of hummocky and swaley cross-stratification— The

817   controlling influence of unidirectional current strength and aggradation rate. Geology 34, 1073.

818   https://doi.org/10.1130/G22930A.1

819   Dunham, R.J., 1962. Classification of Carbonate Rocks According to Depositional Textures 38, 108–

820   121.

821   Elrick, M., 1995. Cyclostratigraphy of Middle Devonian Carbonates of the Eastern Great Basin,

822   Journal of Sedimentary Research. SEPM 65 (1), 61-67

823   Embry, A.F., Klovan, J.E., 1972. Absolute water depth limits of Late Devonian paleoecological zones.

824   Geol. Rundschau 61, 672–686. https://doi.org/10.1007/BF01896340

825

826   Enos, P., 1983. Shelf Environment: Chapter 6. Amer. Ass. Pet. Geol. Stud. Geol. 43, 267–295.
827

828   Eyles, N., Januszczak, N., 2004. "Zipper-rift": a tectonic model for Neoproterozoic glaciations during

829   the breakup of Rodinia after 750 Ma. Earth-Science Rev. 65, 1–73.

830   https://doi.org/10.1016/S0012-8252(03)00080-1

831   Flügel, E., 2004. Microfacies of Carbonate Rocks. Analysis, Interpretation and Application, Berlin,

832   Heidelberg, New York: Springer-Verlag. Cambridge University Press.

833   https://doi.org/10.1017/S0016756806221940

834   Frimmel, H.E., Tack, L., Basei, M.S., Nutman, A.P., Boven, A., 2006. Provenance and

835   chemostratigraphy of the Neoproterozoic West Congolian Group in the Democratic Republic of

836   Congo. J. African Earth Sci. 46, 221–239. https://doi.org/10.1016/j.jafrearsci.2006.04.010

837   Ginsburg, R.N., 1971. Landward Movement of Carbonate Mud: New Model for Regressive Cycles in

838   Carbonates. Amer. Ass. Pet. Geol. Stud. Geol. 55 (2), 340. https://doi.org/10.1306/5D25CE81-

839   16C1-11D7-8645000102C1865D

840   Glumac, B., Walker, K.R., 2000. Carbonate Deposition and Sequence Stratigraphy of the Terminal

841   Cambrian Grand Cycle in the Southern Appalachians, U.S.A. J. Sediment. Res. 70, 952–963.

842   https://doi.org/10.1306/2DC40943-0E47-11D7-8643000102C1865D

843   Hardie, L.A., 1977. Sedimentation on the Modern Carbonate Tidal Flats of north- west Andros Island,

844   Bahamas. Johns Hopkins University Press, 202 pp.

845   Hoffman, P.F., Kaufman, A.J., Halverson, G.P., Schrag, D.P., 1998. A Neoproterozoic snowball

846   Earth. Sciences 281, 1342-1376.

847   Hardie, L.A., Ginsburg, R.N., 1977. Layering; the origin and environmental significance of lamination

848   and thin bedding. In: Sedimentation on the Modern Carbonate Tidal Flats of Northwest Andros

849   Island, Bahamas (Ed. L.A. Hardie), John Hopkins University, Stud. Geol 22, 50–123.

850   Hoffman, P.F., Schrag, D.P., 2002. The snowball Earth hypothesis: testing the limits of global change.

851   Terra Nov. 14, 129–155. https://doi.org/10.1046/j.1365-3121.2002.00408.x

852   James, N.P., Bourque, P.-A., 1992. Reefs and mounds. In: Walker, R.G., James, N.P. (Eds.), Facies

853   Models, Response to Sea Level Change. Geol. Assoc. Canada 1, 323–347.

854   Kampunzu, A.B., Kapenda, D., Manteka, B., 1991. Basic magmatism and geotectonic evolution of the

855   Pan African belt in central Africa: Evidence from the Katangan and West Congolian segments.

856   Tectonophysics 190, 363–371. https://doi.org/10.1016/0040-1951(91)90438-X

857   Keith, B.D., Zuppann, C.W. (eds)., 1993. Mississippian oolites and modern analogs. Amer. Ass. Pet.

858   Geol. Stud. Geol. 35, 265 pp. https://doi.org/10.1306/St35571

859   Kinsmann, D.J.J., 1969. Modes of formation, sedimentary associations and diagnostic features of

860   shallow-water and supratidal evaporites. Bull. Am. Assoc. Petrol. Geol. 53, 830–840.

861

862   Kirschvink, J.L., 1992. Late Proterozoic low-latitude global glaciation: the snowball Earth. In: Schopf,

37

863   J.W., Klein, C., (eds), The Proterozoic biosphere: a multidisciplinary study. Cambridge

864   University Press, Cambridge, 51-52.

865 Kromkamp, J.C., Perkins, R., Dijkman, N., Consalvey, M., Andres, M., Reid, R.P., 2007. Resistance

866   to burial of cyanobacteria in stromatolites. Aquat. Microb. Ecol. 48, 123–130.

867   https://doi.org/10.3354/ame048123

868 Lepersonne, J., 1974. Carte géologique à l'échelle 1/200000. Notice explicative de la feuille Ngungu

869   (Degré carré S6/14 = SB 33.9). République Démocratique du Congo. Département des Mines,

870   Direction du Service Géologique, 61 pp.

871 Li, Z.X., Bogdanova, S.V., Collins, A.S., Davidson, A., De Waele, B., Ernst, R.E., Fitsimons, I.C.W.,

872   Fuck, R.A., Gladkochub, D.P., Jacobs, J., Karlstom, K.E., Lu, S., Natapov, L.M., Pease, V.,

873   Pisarevsky, S.A., Thrane, K., Vernikovsky, V., 2008. Assembly, configuration, and break-up

874   history of Rodinia: a synthesis. Precambrian Research 160 (1–2), 179–210.

875

876 Mamet, B., Préat, A., 2005. Sédimentologie de la série viséenne d'Avesnes-sur-Helpe (Avesnois,

877   Nord de la France). Geol. Belgica 8, 91–107.

878 Monié, P., Bosch, D., Bruguier, O., Vauchez, A., Rolland, Y., Nsungani, P., Buta, N.A., 2012. The

879 late Neoproterozoic/early palaeozoic evolution of the West Congo belt of NW Angola:

880 geochronological (UPb and Ar-Ar) and petrostructural constraints. Terra Nova 24 (3), 1-10.

881

882 Morsilli, M., Pomar, L., 2012. Internal waves vs. surface storm waves: a review on the origin of

883   hummocky cross-stratification. Terra Nov. 24, 273–282. https://doi.org/10.1111/j.1365-

884   3121.2012.01070.x

885 Muanza-Kant, P., Mpiana, Ch, Kanda-Nkula, V., Tack, L., Baudet, D., Archibald, D.B., Glorie, S.,

886   2016. The lower Diamictite Formation of the Cataractes Group, West Congo Supergroup (Bas-

887   Congo, DRC): a 700 Ma marker of extensional episodic activity during breakup of Columbia.,

888   in: 5th International Geologica Belgica 2016 Congress, 26-29 January 2016. University of Mons,

889   Mons, Belgium, P. 57. Abstract Book.

890 Noffke, N., 2010. Geobiology: Microbial mats in sandy deposits from the Archean era to today.

891   Springer. https://doi.org/10.1007/978-3-642-12772-4

38

892   Noffke, N., 2000. Extensive microbial mats and their influences on the erosional and depositional

893   dynamics of a siliciclastic cold water environment (Lower Arenigian, Montagne Noire, France).

894   Sediment. Geol. 136, 207–215. https://doi.org/10.1016/S0037-0738(00)00098-1

895   Patterson, R.J., Kinsman, D.J.J., 1981. Hydrologic Framework of a Sabkha Along Arabian Gulf. Am.

896   Assoc. Pet. Geol. Bull. 65, 1457–1475.

897

898   Pedersen, G.K., 1985. Thin, fine-grained storm layers in a muddy shelf sequence: an example from the

899   Lower Jurassic in the Stenlille 1 well, Denmark. J. Geol. Soc. London. 142, 357–374.

900   https://doi.org/10.1144/gsjgs.142.2.0357

901   Pedrosa-Soares, A.C., Alkmim, F.F., Tack, L., Noce, C.M., Babinski, M., Silva, L.C., Martins-Neto,

902   M.A., 2008. Similarities and differences between the Brazilian and African counterparts of the

903   Neoproterozoic Araçuaí-West Congo orogen. Geol. Soc. London, Spec. Publ. 294, 153–172.

904   https://doi.org/10.1144/SP294.9

905   Pedrosa-Soares, A.C., Alkmin, F.F., 2011. How many rifting events preceded the develop- ment of the

906   Araçuai–West Congo orogen? Geonomos 19 (2), 244–251.

907   Pedrosa-Soares, A.C., Babinski, M., Noce, C., Martins, M., Queiroga, G., Vilela, F., 2011. Chapter 49

908   The Neoproterozoic Macaúbas Group, Araçuaí orogen, SE Brazil. Geol. Soc. London, Mem. 36,

909   523–534. https://doi.org/10.1144/M36.49

910   Perkins, R.G., Kromkamp, J.C., Pamela Reid, R., 2007. Importance of light and oxygen for

911   photochemical reactivation in photosynthetic stromatolite communities after natural sand burial.

912   Mar. Ecol. Prog. Ser. 349, 23–32. https://doi.org/10.3354/meps07087

913   Poidevin, J.L., 2007. Stratigraphie isotopique du strontium et datation des formations carbonatées et

914   glaciogéniques néoprotérozoiques du Nord et de l'Ouest du craton du Congo. Comptes Rendus -

915   Geosci. 339, 259–273. https://doi.org/10.1016/j.crte.2007.02.007

916   Préat, A., Delpomdor, F., Ackouala Mfere, A.P., Callec, Y., 2018. Paleoenvironments, $\delta13C$ and $\delta18O$

917   signatures in the Neoproterozoic carbonates of the Comba Basin, Republic of Congo:

918   Implications for regional correlations and Marinoan event. J. African Earth Sci. 137, 69–90.

919   https://doi.org/10.1016/j.jafrearsci.2017.09.002

920   Préat, A., Kolo, K., Prian, J.-P., Delpomdor, F., 2010. A peritidal evaporite environment in the

921   Neoproterozoic of South Gabon (Schisto-Calcaire Subgroup, Nyanga Basin). Precambrian Res.

922   177, 253–265. https://doi.org/10.1016/J.PRECAMRES.2009.12.003

923   Préat, A.R., Delpomdor, F., Kolo, K., Gillan, D.C., Prian, J.-P., 2011. Stromatolites and

924   Cyanobacterial Mats in Peritidal Evaporative Environments in the Neoproterozoic of Bas-Congo

925   (Democratic Republic of Congo) and South Gabon. Springer, Dordrecht, pp. 43–63.

926   https://doi.org/10.1007/978-94-007-0397-1_3

927   Sarkar, S., Bose, P.K., 1992. Variations in Late Proterozoic stromatolites over a transition from basin

928   plain to nearshore subtidal zone. Precambrian Res. 56, 139–157. https://doi.org/10.1016/0301-

929   9268(92)90088-6

930   Satterley, A.K., 1996. The interpretation of cyclic successions of the Middle and Upper Triassic of the

931   Northern and Southern Alps. Earth-Science Rev. 40, 181–207. https://doi.org/10.1016/0012-

932   8252(95)00063-1

933

934   Scholle, P.A., Kinsman, D.J.J., 1974. Aragonitic and High-Mg Calcite Caliche from the Persian Gulf--
935   A Modern Analog for the Permian of Texas and New Mexico. J. Sediment. Res. 44, 904–916.
936   https://doi.org/10.1306/212F6BD6-2B24-11D7-8648000102C1865D
937
938   Sellwood, B.W., 1986. Shallow-marine carbonate environ- ments. In: H.G. Reading (Editor),
939   Sedimentary Environ- ments and Facies. Blackwell, 2nd ed. 283 342.
940
941   Shearman, D.J., 1963. Recent anhydrite, gypsum, dolomite and halite fromthe coastal flat of the

942   Arabian shore of the Persian Gulf. Proc. Geol. Soc. Lond. 1607/63, 5

943

944   Schermerhorn, L.J.G., Stanton, W.I., 1963. Tilloids in the West Congo geosyncline. Q. J. Geol. Soc.

945   119, 201–241. https://doi.org/10.1144/gsjgs.119.1.0201

946

947   Shukla, V., Friedman, G.M., 1981. An unusual occurrence of surficial anhydrite in a moist temperate

948   zone: Example from the Lockport Formation (Middle Silurian) of New York. Sediment. Geol.

949   29, 125–131. https://doi.org/10.1016/0037-0738(81)90003-8

950   Sibley, D.F., Gregg, J.., 1987. Classification of Dolomite Rock Textures. J. Sediment. Res. Vol. 57,

951   967–975. https://doi.org/10.1306/212F8CBA-2B24-11D7-8648000102C1865D

952   Sikorski, J., 1958. Echelle stratigraphique provisoire des étages C1-C2-C3 du système Schisto-

953   Calcaire du Bas-Congo. CIMINGA, note n°15.

954   Straathof, G.B., 2011. Neoproterozoic low latitude glaciations: an african perspective. The University

955   of Edinburgh.

956   Strasser, A., 2016. Hiatuses and condensation: an estimation of time lost on a shallow carbonate

957   platform. Depos. Rec. 1, 91–117. https://doi.org/10.1002/dep2.9

958   Strasser, A., 1991. Lagoonal-peritidal sequences in carbonate environments: autocyclic and allocyclic

959   processes. In: Einsele G, Ricken W, Seilacher A (Eds), Cycles and events in stratigraphy.

960   Springer, Berlin, 709–721.

961   Tack, L., Wingate, M.T.., Liégeois, J.-P., Fernandez-Alonso, M., Deblond, A., 2001. Early

962   Neoproterozoic magmatism (1000–910 Ma) of the Zadinian and Mayumbian Groups (Bas-

963   Congo): onset of Rodinia rifting at the western edge of the Congo craton. Precambrian Res. 110,

964   277–306. https://doi.org/10.1016/S0301-9268(01)00192-9

965

966   Tack, L., De Grave, J., Burgess, R., Baudet, D., Fernandez-Alonso, M., Kongota-Isasi, E., Nseka-

967   Mbemba, P., Delvaux, D., 2018. 525 Ma riebeckite in a quartz vein into the Noqui granite: evidence

968   for a late Pan African extensional event in the West Congo Belt (Matadi area, Bas-Congo region, DR

969   Congo). 17th Conference of the Geological Society of Africa and 27th Colloquium of African

970   Geology. Aveiro, Portugal.

971

972   Tait, J., Delpomdor, F., Preat, A., Tack, L., Straathof, G., Nkula, V.K., 2011. Chapter 13

973   Neoproterozoic sequences of the West Congo and Lindi/Ubangi Supergroups in the Congo

974   Craton, Central Africa. Geol. Soc. London, Mem. 36, 185–194. https://doi.org/10.1144/M36.13

975   Thiéblemont, D., Castaing, C., Billa, M., Bouton, P., Préat, A., 2009. Notice explicative de la carte

976   géologique et des ressources minérales de la République Gabonaise à 1/1000000. Program.

977   Sysmin 8 ACP GA 017 384pp.

978   Trompette, R., Boudzoumou, F., 1988. Palaeogeographic significance of stromatolitic buildups on

979   Late Proterozoic platforms: The example of the West Congo basin. Palaeogeogr. Palaeoclimatol.

980   Palaeoecol. 66, 101–112. https://doi.org/10.1016/0031-0182(88)90083-1

981   Tucker, M.E., Wright, V.P., Dickson, J.A.D., Wiley InterScience (Online service), 1990. Carbonate

982   sedimentology. Blackwell Scientific Publications.

983   Tucker, M.E., Wright, V.P., 1990. Carbonate Sedimentology. Blackwell Scientific Publications,
984   Oxford, 482 pp.
985

986   Uhlein, G.J., Uhlein, A., Pereira, E., Caxito, F.A., Okubo, J., Warren, L. V., Sial, A.N., 2019.

987   Ediacaran paleoenvironmental changes recorded in the mixed carbonate-siliciclastic Bambuí

988   Basin, Brazil. Palaeogeogr. Palaeoclimatol. Palaeoecol. 517, 39–51.

989   https://doi.org/10.1016/j.palaeo.2018.12.022

990   Walker, R.G. and Plint, A.G., 1992. Wave-and Storm-Dominated Shallow Marine Systems. In:

991   Walker, R.G. and James, N.P., Eds., Facies Models: Response to Sea Level Change. Geol.

992   Assoc. Canada, Newfoundl. 219–238.

993   Wang, J., Li, Z.-X., 2003. History of Neoproterozoic rift basins in South China: implications for

994   Rodinia break-up. Precambrian Res. 122, 141–158. https://doi.org/10.1016/S0301-

995   9268(02)00209-7

996

997   Young, G.M., 1995. Are Neoproterozoic glacial deposits preserved on the margins of Laurentia
998   related to the fragmentation of two supercontinents? Geology 23, 153.
999   https://doi.org/10.1130/0091-7613(1995)023<0153:ANGDPO>2.3.CO;2
1000

1001

1002   **Table 1** Location (latitude, longitude and elevation) of the identified outcrops in the studied

1003   area. Most of the outcrops have been described in this study. See Fig. 1, Fig. 16 and text for

1004   details.

1005

1006   **Table 2** Summary of facies associations (FA) and facies (F) defined in the SCI$_c$ Formation with

1007   descriptions and environmental interpretations.

1008

42

1009   **Table 3** Cycle features of SCI$_c$ Formation in the studied area.

1010

1011   **Table 4** Detailed description of D and Saris sections

1012

1013   **Figure 1** Location map of the Neoproterozoic West Congo Basin (NWCB) divided into Niari-Nyanga,

1014   Comba, Lower Congo and North Angola (NA) subbasins. The Niari-Nyanga, Lower Congo and North

1015   Angola subbasins record sedimentation on a passive margin of the Congo Craton, and the Comba

1016   subbasin belongs to the SE margin of the Sangha aulacogen.

1017

1018   **Figure 2** Comparative lithostratigraphy between the West Congolian Supergroup in RC and the West

1019   Congo Supergroup in DRC. In RC, the stratigraphy of the West Congolian Supergroup has been

1020   recently revised by Charles et al. (2015). In DRC, the Lukala Subgroup, formerly Schisto-Calcaire

1021   Subgroup, is divided into five formations (C1 to C5), which are stratigraphically equivalent with the

1022   SCI Formation – correlated with the C1 to C3 formations of Lower Congo subbasin, SCII Formation –

1023   correlated with the C4 Formation of Lower Congo subbasin, and SCIII Formation – correlated with

1024   the C5 Formation of Lower Congo subbasin. Sr is based on worldwide ^{87}Sr/^{86}Sr composition of

1025   seawater during the Neoproterozoic (1000-542 Ma) Era.

1026

1027   **Figure 3** Simplified geological map showing location of the identified outcrops (L1, U and T to

1028   Zanzo, V, W and X from East to West). No sections have been described for A, E, L1, U, V, W, X and

1029   Y in this study. See Fig. 16 for description of each section.

1030

1031   **Figure 4** Field and thin-section photographs of homogeneous clayey mudstones and laminar silty

1032   mudstones (F1) in the SCI$_c$ Formation. **(A)** Alternations of darker and purplish layers consisting of

1033   clayey silty carbonates and microbial mudstones overlain by a domal stromatolite (in the background).

1034   The domal stromatolite represents the lower part of a complex zone of giant stromatolites (15-20 m in

1035   height), section D. **(B, C, D)** Planar and undulating platy limestones (3-5 cm-thick) showing

1036   alternations of homogeneous carbonate muds and slightly laminar silty mudstones identified as MISS

1037   (Microbial Induced Sedimentary Structures) by petrographic description, D and O sections. **(E)**

1038   Microbial mats (dark laminations or MISS undulating levels) within a fine microsparitic matrix.

1039   Quartz, feldspars and pyrite are recognized within the matrix or overlie the microbial mats, section D.

1040   **(F)** Dark bacterial filament in a microsparitic matrix, section D.

1041

1042   **Figure 5** Field photographs of the stromatolitic facies (F2 and F6) in the SCI$_c$ Formation. **(A)** Upper

1043   part of a giant domal stromatolite with 4-5 m in width, section H. **(B)** Columnar stromatolite with

1044   parallel columns, section P. **(C)** Centimetric alternations of grey planar microbial mats and

1045   accumulations of coarse-grained stromatoclasts forming radial-bundles, section F. **(D)** Giant "cigare"

1046   or coned-shaped stromatolite (10- 15 m in length), section F . **(E)** Wavy and planar microbial mats,

1047   section M . **(F)** Small domal stromatolite overlying or laterally relayed by planar microbial mats,

1048   section D. **(G)** Succession of domal stromatolites in the top of a stromatolitic bioherm (15-20 m in

1049   height), section H.

1050

1051   **Figure 6** Sedimentary features of the oolite grainstones in the SCI$_c$ Formation. **(A)** Bidirectional low-

1052   angle planar laminations with low-angle truncations, section I. **(B)** Sets of trough-stratifications,

1053   section I. **(C)** Mega-ripples, cross-laminations showing herringbone stratifications, section C. **(D)**

1054   Mega-ripples showing hummocks and swales with low-angle laminations, section C. **(E)** Mega-ripples

1055   with hummocks (see arrow) showing SCS when the top of the hummocks has been eroded. Stylolites

1056   (lower part of the picture) are well developed, with high amplitude, as is generally the case in all the

1057   oolitic grainstones, section I. **(F, G)** HCS with furrows showing flat (less) and hollow (more) bottoms

1058   passing in the upper part to mega-ripples (cross-laminations), section S. **(H)** Oolite grainstones (F3a)

1059   overlying columnar stromatolites (F2), irregular contact between F3a and F2 with thick oolite beds

1060   overlying giant stromatolite, section T.

1061

1062   **Figure 7** Thin-section and field photographs of the oolitic grainstones-floatstones (F3a and F3b) in the

1063   SCI$_c$ Formation**. (A)** Grainstone showing well-sorted spherical oolites (F3a) with both concentric and

1064   radial structures. Cementation consists of isopachous lamellar calcite and blocky calcite, section

1065   MAD8017. **(B)** Well represented cementation filling the intergranular porosity in an oolite grainstone

1066   (F3a). As described later, the cementation consists of isopachous lamellar calcite and a blocky calcite,

1067   section MAD8018. **(C)** Asymmetric oolite with a concentric cortex and coarse-grained slightly

1068   rosette-like nuclei, section I. **(D)** Greyish floatstone with dominant aggregates, see (F) for facies

1069   description, section MAD8018. **(E)** Part of centimetric grapestone in a floatstone ooid-aggregate

1070   (F3b), the grapestone consists of micritized ooids bounded together by a microsparitic matrix, section

1071   I. **(F)** Millimetric aggregates in a floatstone or 'false' rudstone, see (D) for the field photograph,

1072   section I. **(G)** Asymmetric oolites (see black arrows) in a grainstone with equant calcite, section

1073   MAD8017. **(H)** Asymmetric oolite (see black arrow) in a grapestone. The asymmetric oolite appears

1074   to be reworked before bounded with other oolites to build the grapestone, as shown by the orientation,

45

1075   section MAD8017.

1076

1077   **Figure 8** Thin-section and field photographs of lagoonal facies (F3c) and intraformational

1078   conglomerate (F4) in the SCI$_c$ Formation. **(A)** Peloidal grainstone-packstone with micritic oolites and

1079   relics of larger oolites exhibiting a fine concentric structure in the outer part of the cortex, section

1080   MAD8018. **(B**) Peloidal packstone without micritic oolites or larger concentric oolites as described

1081   previously**,** section MAD8018. **(C and E)** Homogeneous mudstone with pyrite and oxidized organic

1082   matter relics (see arrow in C), section MAD8016. **(D)** Succession of centimetric beds of greyish

1083   homogeneous mudstones, section MAD8019. **(F)** Peloidal grainstone showing herringbone cross-

1084   stratifications, top of Saris Section (MAD8017). **(G)** Intraformational conglomerate showing

1085   elongated mud-clasts and oolites relics with vadose cementation, section B. **(H)** Intraformational

1086   conglomerate with plurimillimetric and inframillimetric mud-clasts. The larger ones are elongated and

1087   affected by vertical cracks, section MAD8017.

1088

1089   **Figure 9** Thin-section and field photographs of peritidal facies (F3d, F4 and F6) in the SCI$_c$

1090   Formation. **(A)** Reddish floatstone with abundant pisoids, Sonocc section. See (B) and (C) for the

1091   microfacies description. **(B, C)** Plurimillimetric pisoids showing a fine concentric structure, the

1092   nucleus is micritic and partly replaced by a coarse calcite (B) and consists of oolites (C). **(D)**

1093   Millimetric asymmetric oolites oriented in opposite directions in a pisoid floatstone. The asymmetric

1094   oolites show a concentric cortex with a coarse granular calcite nucleus, Sonocc section. **(E)**

1095   Inframillimetric alternations of planar microbial mats and peloid packstone. Note that peloids (in the

1096   lower part) show circular cracks, Sonocc section. **(F)** Calcitized anhydrite rosette in a peloidal

46

1097   bindstone, MAD8017 section. **(G)** Parts of centimetric mud-clasts interlayered by microbial mats

1098   relics, MAD8017 section. **(H)** Spiny (left) and half-moon oolites (right) in a floatstone

1099   intraformational conglomerate with abundant micritic oolites, MAD8017 section.

1100

1101   **Figure 10** Thin-section and field photographs of the fine-grained laminar detrital mudstones (F5) in

1102   the SCI$_c$ Formation. **(A)** Pluricentimetric alternations of grey-light oolite grainstones (F3a) and fine-

1103   grained laminar detrital mudstones (F5), section F. **(B)** Fine-grained laminar detrital mudstones (F5)

1104   topped by a brecciated bindstone microbial mats (F6) showing random stromatoclasts building slightly

1105   radial bundles structures, section J. **(C)** Thin low-angle light-colored laminae (silty fine sand to fine

1106   silt) interlayered by dark-colored laminae. Light-colored laminae are enriched in quartz, feldspars,

1107   clays minerals, calcite and dolomite crystals (see D). Dark-colored laminae display a pyrite-rich

1108   homogeneous mudstone, section F. **(D)** Quartz, feldspars, clinochlore (greenish crystal), pyrite and

1109   xeno-to hypidiotopic calcite and dolomite crystals in a light-colored laminae of F5, section F.

1110

1111   **Figure 11** Thin section and field photographs of the evaporative dolomudstones (F7) in the SCI$_c$

1112   Formation. **(A, B and C)** Reddish and yellowish dolomudstone with abundant rosettes and laths of

1113   evaporative minerals, top of Sonocc section. See Figs. D to G for the microfacies description. **(D and**

1114   **E)** Rosettes and laths of anhydrite now calcitized, the matrix is a slightly microsparitized

1115   dolomudstone. **(F)** Nodule of well-preserved anhydrite partly silicified. **(G)** Evaporative

1116   dolomudstone showing abundant fenestrae testifying vadose conditions.

1117

1118 **Figure 12** Revised sedimentary model of the SCI$_c$ Formation in the Niari-Nyanga and Comba

1119 sections of the NWCB in RC from outer-ramp with MISS (FA1) to supratidal sabkha (FA5).

1120 Facies associations (FA1 to FA5) represent the standard sequence of the studied formation

1121 (see Table 2 for explanation). The previous sedimentary model has been described in Préat et

1122 al. (2018).

1123

1124 **Figure 13** Types of cycles (D *vs* S) with their facies (F1-F7) successions in the SCI$_c$

1125 Formation, showing shallowing upward trends.'D4 is for 'Deep cyles', 'S' is for Shallow

1126 cycles'. See Table 3 for explanation

1127

1128 **Figure 14** Stratigraphic section of the active Saris (MAD8017) quarry exposing the SCI$_c$ Formation,

1129 showing sample location (8017-1 to 8017-22), lithologic curve (from F1 to F7 facies),

1130 sedimentological features and stacking patterns. Explanations in text, for location see Fig. 1. FAS=

1131 facies successions, PSQ= parasequence, PSQS= parasequence set, Prog. = progradation, Aggr. =

1132 aggradation. M = mudstone, W = wackestone, P = packstone, G = grainstone, R = rudstone, B =

1133 boundstone.

1134

1135 **Figure 15** Stratigraphic section of the inactive D quarry exposing the SCI$_c$ Formation, sample location

1136 (D1 to D85), lithologic curve (from F1 to F7 facies), sedimentological features and stacking patterns.

1137 Explanations in text, for location see Fig. 1. FAS= facies successions, PSQ= parasequence, PSQS=

1138 parasequence set, Prog. = progradation, Aggr. = aggradation. M = mudstone, W = wackestone, P =

1139 packstone, G = grainstone, R = rudstone, B = boundstone.

48

1140

1141

1142 **Figure 16** Stratigraphic correlation of the studied sections based on the stratigraphic key surfaces (TS

1143 and MFS) and the lithofacies associations. See also Fig. 1 for location of sections T to MAD8019

1144 (Zanzo). Sections U to Y are not represented here.

1145 TS = transgressive surface represented by a heavy red line, MFS = maximum flooding surface

1146 represented by a heavy dark line. Filled and unfilled arrows represent respectively complete and

1147 uncomplete aggradational phases in TST (transgressive system tract) sedimentation. TS =

1148 transgressive surface, MFS = maximum flooding surface. See text and Fig. 17 for details. Dark

1149 arrows= aggradation (sections K, H, D, B and Zanzo).

1150

1151 **Figure 17** Tentative sequence stratigraphic correlation of the SCI Subgroup between the

1152 Niari-Nyanga and Comba subbasins (RC) and Lower Congo subbasin (RDC) with two

1153 transgressive-regressive third-order sequences. The TST sedimentation is recorded in the

1154 SCIa and the lower SCIb in RC, and in the C1 Formation and C2a and C2b members in DRC.

1155 The SCIb in RC, and its stratigraphic coeval C2c to C2e members in DRC is marked by a

1156 HST phase. The SCIb-SCIc transition is characterized by a LST sedimentation of shallow

1157 water deposits (FA3/FA4, with abundant S2 cycles), which is also recorded in the C2f to C2h

1158 members in DRC. The LST phase is topped by a transgressive surface (TS) leading to TST

1159 sedimentation ('deep' MISS facies) until the maximum flooding surface (MFS) initiating the

1160 HST sedimentation with giant stromatolites, which are coeval with the C3a Member in DRC.

1161 The top of the SCI$_c$, and its stratigraphic equivalent C3b Member in DRC, is marked by

49

1162   deposition of silty evaporites (LST) at the transition SCI-SCII. TS, MFS and SB (sequence

1163   boundaries) are indicated respectively by heavy dark and red lines. LST = lowstand system

1164   tract, TST = transgressive system tract, HST = highstand system tract, FRST= Forced

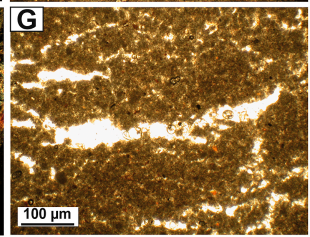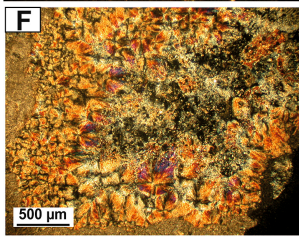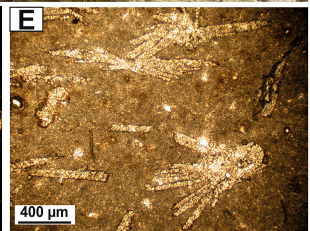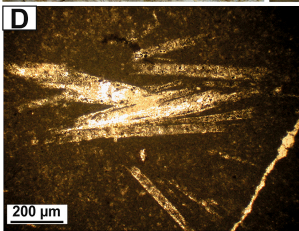1165   regression system tract.

1166

1167
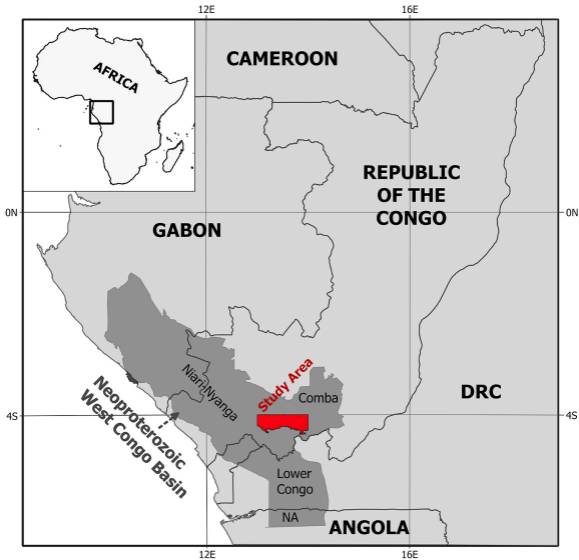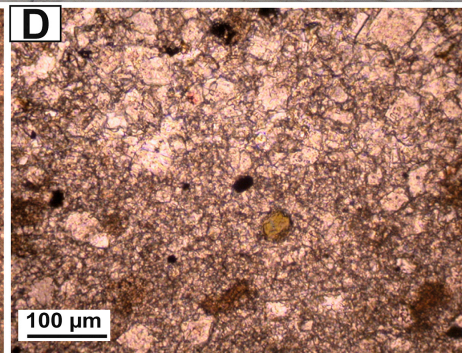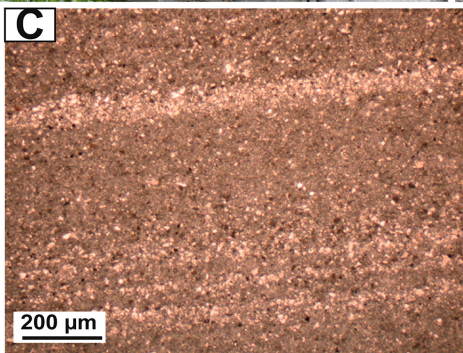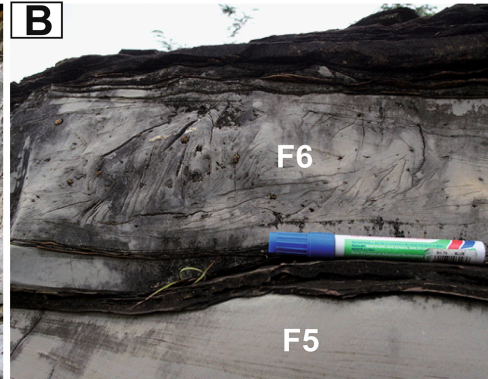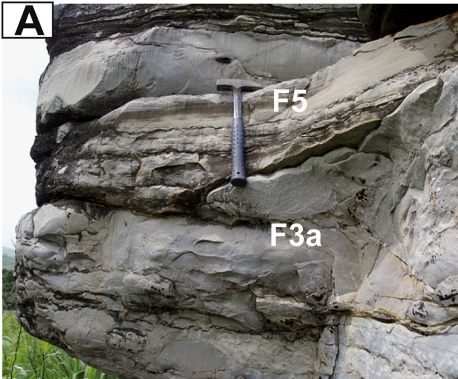
Inset map shows AFRICA with a box indicating the study region.

Labels on main map:
CAMEROON
REPUBLIC OF THE CONGO
GABON
DRC
ANGOLA
Niari/Nyanga
Study Area
Comba
Lower Congo
NA
Neoproterozoic West Congo Basin

Coordinate labels: 12E, 16E, 0N, 4S

SCIc Formation - Niari-Nyanga/Comba Subbasins - Neoproterozoic West Congo Basin - Republic of Congo
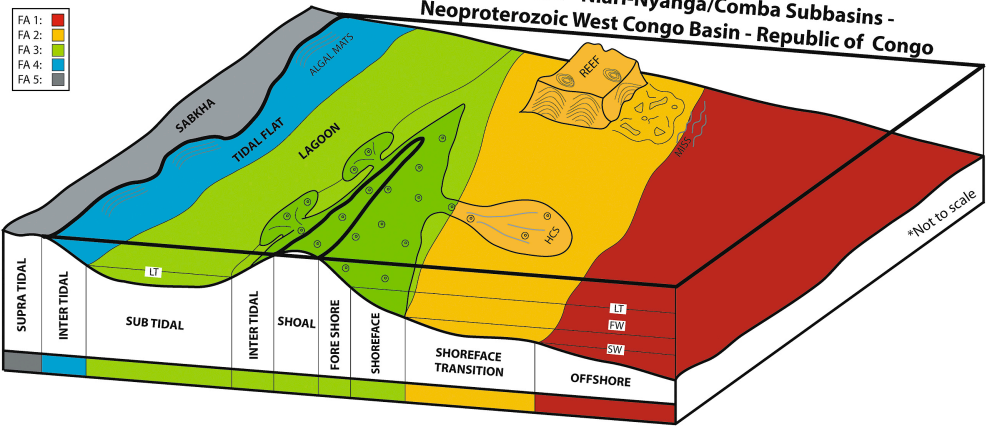
Peritidal cycles

Cycle S1

	M W P G R B
F7	✳✳ ✳✳
F6	
F5	
F4	⊙
F3c	• • •
F3b	⬭⬭⬭
F3a	⬭⬭

Cycle S2

	M W P G R B
F7	✳✳ ✳✳
F6	
F5	
F4	
F3c	⋎ ≠

Cycle S3

	M W P G R B
F7	✳✳ ✳✳
F6	
F5	
F4	
F3d	⬭⬭⬭

Deep cycles

Cycle D1

	M W P G R B
F6	
F5	
F4	
F3	
F2	
F1	
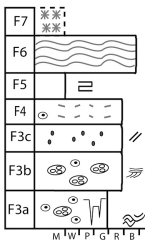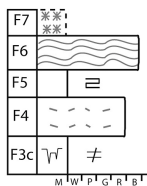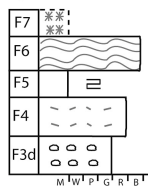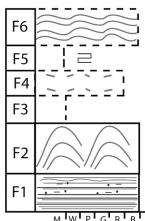
Cycle D2

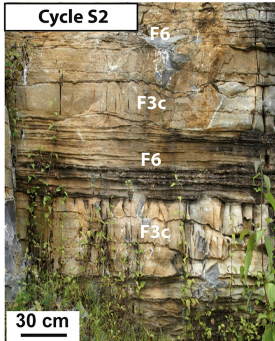|	M W P G R B
F6	
F5	
F4	
F3	
F2	
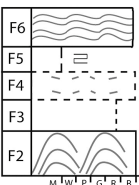
Legend

- ⊙ Oolite
- ⬭ Pisoid
- • Peloid / micritic ooid
- ⬭⬭ Aggregate
- ⌢⌢ Domal Stromatolite
- ⌣⌣ Intraformational conglomerate
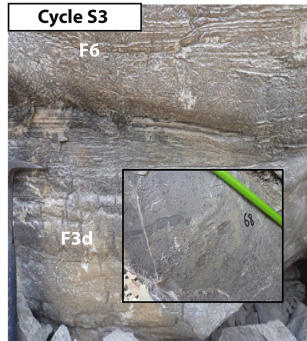- ∼∼ Planar stromatolite
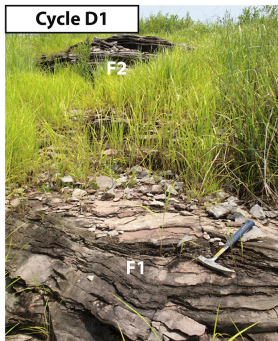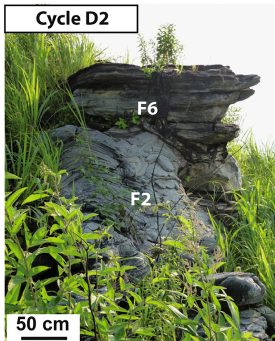- ✳ Evaporite

Cycle S1 — F3a, F5, F3a

Cycle S2 — F6, F3c, F6, F3c — 30 cm

Cycle S3 — F6, F3d — 68

Cycle D1 — F2, F1

Cycle D2 — F6, F2 — 50 cm
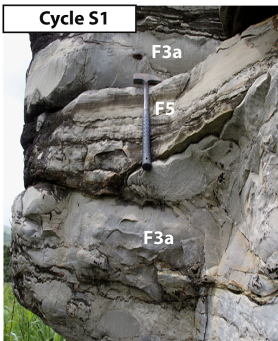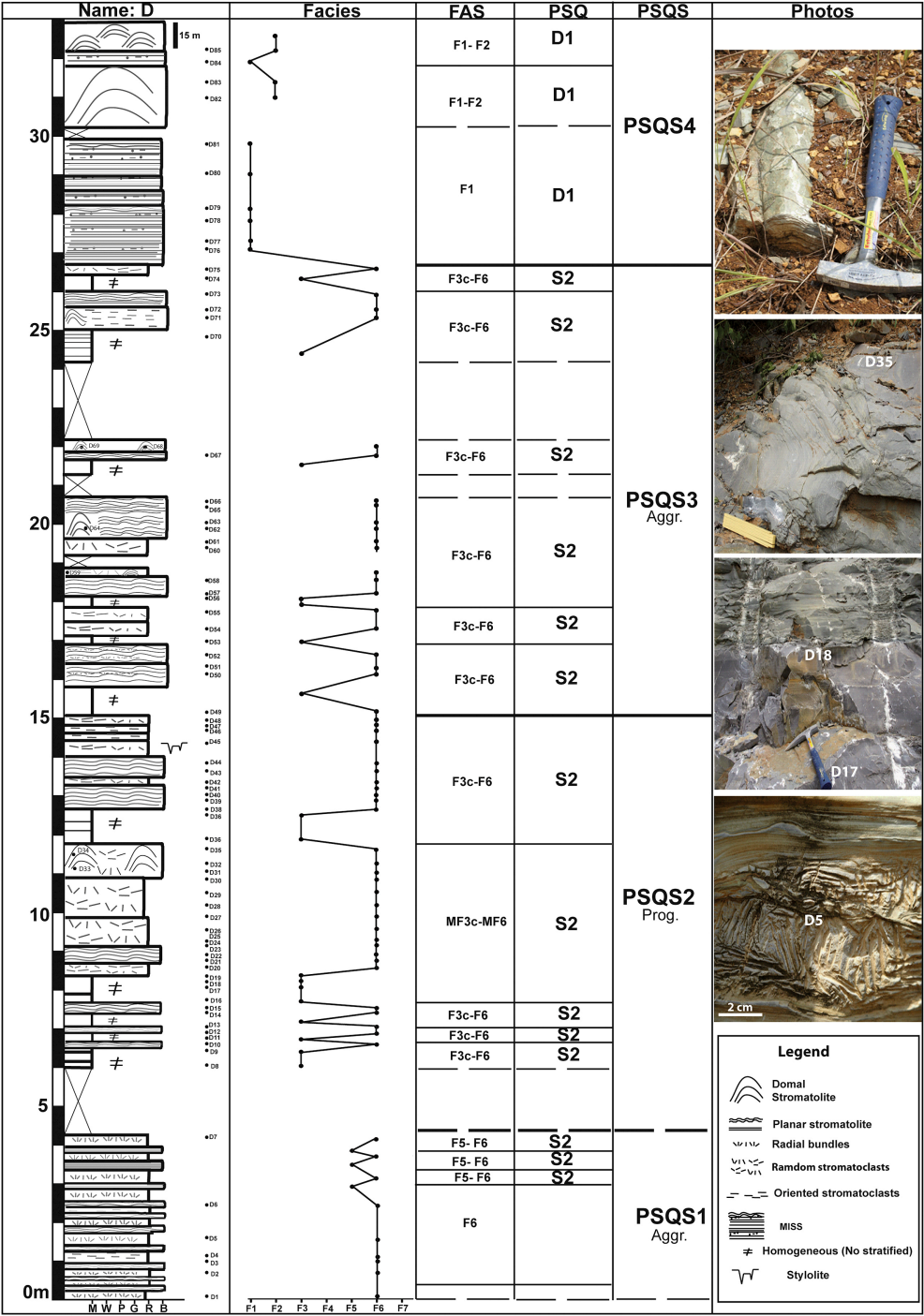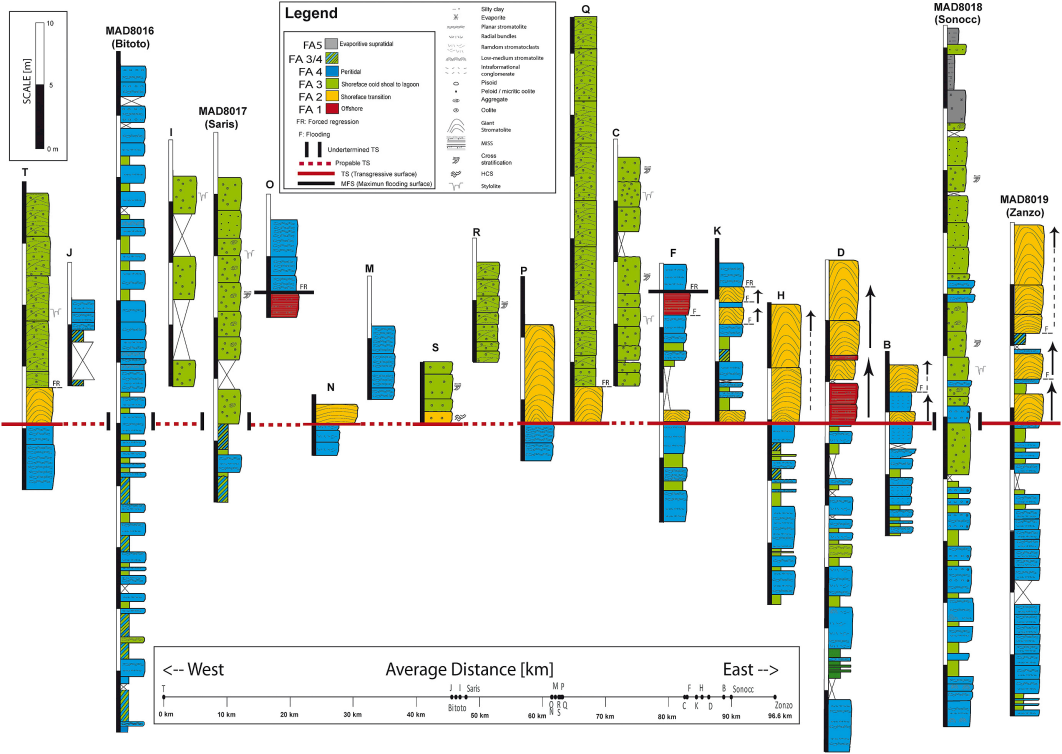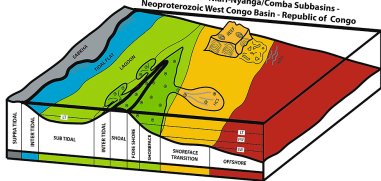
Legend

- ≈ Hummocky cross stratification
- ⫽ Cross stratification
- ⊒ Planar stratification
- ≠ No stratified (homogeneous)
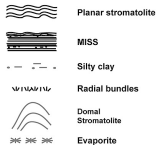- ⫽ Angular stratification
- ⌄⌄ Stylolite

MAD 8017 (Saris) | Facies | FAS | PSQ | PSQS | Photos

Photo panels
8017-21 — 100 µm
8017-17 — 250 µm
8017-15 — 100 µm
8017-14 — 500 µm
8017-13 — 250 µm
8017-6 — 200 µm
8017-1 — 150 µm

Depth scale (m): 25, 20, 15, 10, 5, 0m

Sample labels: 8017-22, 8017-21, 8017-20, 8017-19, 8017-18, 8017-17, 8017-16, 8017-15, 8017-14, 8017-13, 8017-12, 8017-11, 8017-10, 8017-9, 8017-8, 8017-7, 8017-6, 8017-5, 8017-4, 8017-3, 8017-2, 8017-1

Facies axis: F3a F3b F3c F4 F5 F6 F7

Lithology axis: M W P G R B

FAS	PSQ	PSQS
F3a	S1	PSQS3
F3a-F3c	S1	
F3a-F3b	S1	
F3a-F3b	S1	
F3c-F4	S2 x 6	PSQS2 Aggr.
F3c-F4	S2	PSQS1 Prog.
F3c-F4	S2	
F3c-F6	S2	
F3c-F4-F6	S2	
F3c-F4	S2	
F3c-F4	S2	
F3c-F6	S2	
F3c-F6	S2	

Legend

- ⊙ Oolite
- • Peloid /micritic ooid
- ⬡ Aggregate
- ⌒ Domal Stromatolite
- Intraformational conglomerate
- Planar stromatolite
- Radial bundles
- Oriented stromatoclasts
- Erosive contact
- Cross stratification
- Planar stratification
- Angular stratification
- No stratified (homogeneous)
- Stylolite
- Gutter cast

Stratigraphic column "Name: D" showing columns for Facies, FAS, PSQ, PSQS, and Photos.

Name: D	Facies	FAS	PSQ	PSQS	Photos
		F1-F2	D1	PSQS4	
		F1-F2	D1		
30		F1	D1		
		F3c-F6	S2		
		F3c-F6	S2	PSQS3 Aggr.	
25		F3c-F6	S2		D35
		F3c-F6	S2		
20		F3c-F6	S2		
		F3c-F6	S2		D18
		F3c-F6	S2		D17
15		F3c-F6	S2		
		MF3c-MF6	S2	PSQS2 Prog.	D5
10		F3c-F6	S2		
		F3c-F6	S2		
		F3c-F6	S2		
5		F5-F6	S2		
		F5-F6	S2		
		F5-F6	S2		
		F6		PSQS1 Aggr.	
0m					

Legend:
- Domal Stromatolite
- Planar stromatolite
- Radial bundles
- Ramdom stromatoclasts
- Oriented stromatoclasts
- MISS
- Homogeneous (No stratified)
- Stylolite

Legend

FA5 — Evaporitic supratidal

FA 3/4

FA 4 — Peritidal

FA 3 — Shoreface oolid shoal to lagoon

FA 2 — Shoreface transition

FA 1 — Offshore

FR: Forced regression

F: Flooding

— Undetermined TS

— Probable TS

— TS (Transgressive surface)

— MFS (Maximum flooding surface)

Silty clay
Evaporite
Planar stromatolite
Radial bundles
Random stromatoclasts
Low-medium stromatolite
Intraformational conglomerate
Pisoid
Peloid / micritic oolite
Aggregate
Oolite
Giant Stromatolite
MFS
Cross stratification
HCS
Stylolite

MAD8016 (Bitoto)

MAD8017 (Saris)

MAD8018 (Sonocc)

MAD8019 (Zanzo)

SCALE [m] — 10, 5, 0 m

T J I O M N S R P Q C F K H D B

<-- West   Average Distance [km]   East -->

0 km   10 km   20 km   30 km   40 km   50 km   60 km   70 km   80 km   90 km   96.6 km

T   J I Saris   M P   F H   B Sonocc
         Bitoto   60 km Q R Q   K D   90 km Zanzo
                          N S   96.6 km

SCIc Formation - Niari-Nyanga/Comba Subbasins - Neoproterozoic West Congo Basin - Republic of Congo

Legend

- 〰️ Planar stromatolite
- ≣ MISS
- ‐ ‐ ‐ Silty clay
- Ⅶ Radial bundles
- ⌒ Domal Stromatolite
- ⋇ Evaporite

Formation/Member | Lithology | Third-order sequence

RC	DRC		
SCIIa	C4a		LST
			SB
SCIc	C3b		FRST
			FRS
	C3a		HST
			MFS / TST
	C2f-C2h		LST
			SB
SCIb	C2c-C2e		HST
			MFS
	C2a-C2b		TST
SCIa	C1		

25 m

F3a

F2

50 cm

C

B

A

Period	Age	Event	Republic of the Congo Group	Subgroup	Formation	Democratic Republic of the Congo Group	Subgroup	Formation	Member	Geochronology
Cambrian (?)		Pan African Orogeny	Mpioka	MPII	MPIIc	Mpioka	PII	P3	P3b	Ar-Ar: 490±3 Ma(9)
					MPIIb				P3a	K-Ar: 499±19 Ma(8)
					MPIIa					Ar-Ar: 524.6±4.6 Ma(7)
								P2		U-Pb: ~540 Ma(9)
				MPI	MPIc		PI	P1	P1c	Pb-Pb: 558±59 Ma(3)
					MPIb				P1b	
					MPIa				P1a	Pan-African orogeny Ar-Ar: 566±42 Ma(3)
	541 Ma	Neoproterozoic oxygenation			MP0			P0		
Neoproterozoic III (Ediacaran)			Schisto-Calcaire	SCIII	SCIIIc	Lukala (Schisto-Calcaire)	CIII	C5	Upper C5b	
					SCIIIb				C5b	
					SCIIIa				C5a	
		Gaskier Glaciation		SCII	SCIIc		CII	C4	C4c	87Sr/86Sr: ~575 Ma(4)
					SCIIb				C4b	
					SCIIa				C4a	
				SCI	SCIc		CI	C3	C3b	
					SCIb				C3a	
		Marinoan Glaciation			SCIa			C2	C2a to C2h	
	635 Ma							C1		
			Niari Group (Upper Diamictite)			Haut Shiloango	ShII	Upper Diamictite		U-Pb: 707±23 Ma(2)
Neoproterozoic II (Cryogenian)			Mayumbe	Louila/Bouenza	Lo — Bz4			Sh8	Sh8a to Sh8i	87Sr/86Sr: ~645 Ma(4)
					Bz3			Sh7		
					Bz2			Sh6		Pb-Pb: ~650 Ma(3)
					Bz1			Sh5		
							ShI	Sh4		
								Sh2-3		
								Sh1		
		Sturtian Glaciation			Lower Diamictite	Sansikwa		Lower Diamictite		U-Pb: 694±4 Ma(2)
										U-Pb: 713±49 Ma(5)
	720 Ma			Mossouva	Mo 2			S3		Pb-Pb: 923±43 Ma(3)
Neoproterozoic I (Tonian)		Bitter Springs anomaly			Mo1			S2		
								S1		U-Pb: 912±7 Ma(1)
			Sounda	Mvouti	Mvo 3			S0		
					Mvo 2					
		Rifting			Mvo 1					
				Kakamoéka	Kak 2	Tshela/Seke-Banza (Mayumbian)				U-Pb: 867±4 Ma(5)
					Kak 1					U-Pb: 904±6 Ma(5)
				Nemba	MaFc	Nzadi (Zadinian)				U-Pb: 906±6 Ma(6)
	1000 Ma									U-Pb: 999±7 Ma(1)
Archean-Paleoproterozoic basement										

West Congolian Supergroup (Republic of the Congo) / West Congo Supergroup (Democratic Republic of the Congo)

Cataractes (West Congolian)
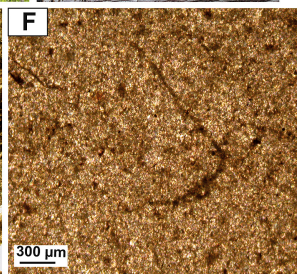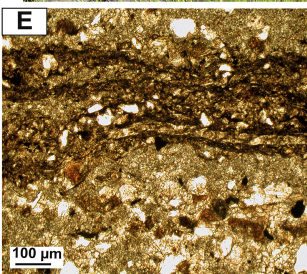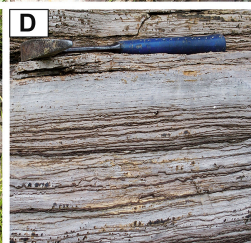
(1) Tack et al. (2001), (2) Straathof (2011), (3) Frimmel et al. (2006), (4) Poidevin (2007), (5) Thiéblemont et al. (2009), (6) Charles et al. (2015), (7) Tack et al. (2018), (8) Fullgraff et al. (2015), (9) Monié et al. (2012)
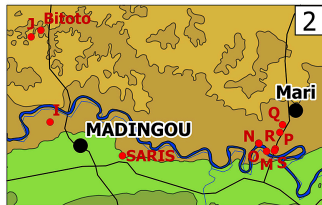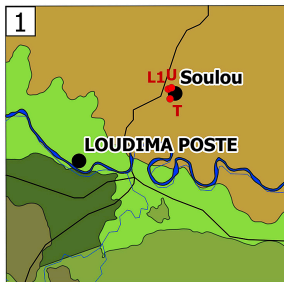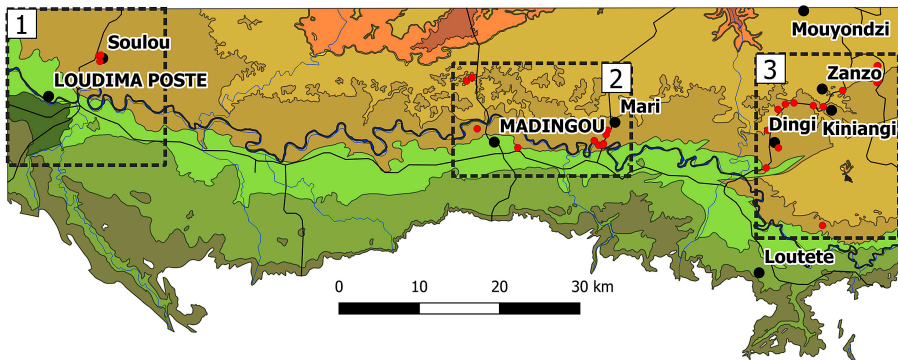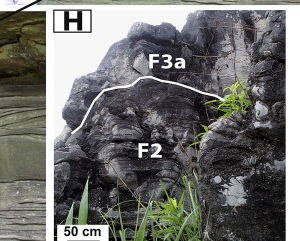
F3a

F2

50 cm

A. 1 mm

B. 250 µm
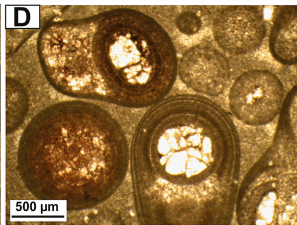
C. 100 µm

D.

E. 300 µm

F. 500 µm

G. 500 µm

H. 250 µm

A-H
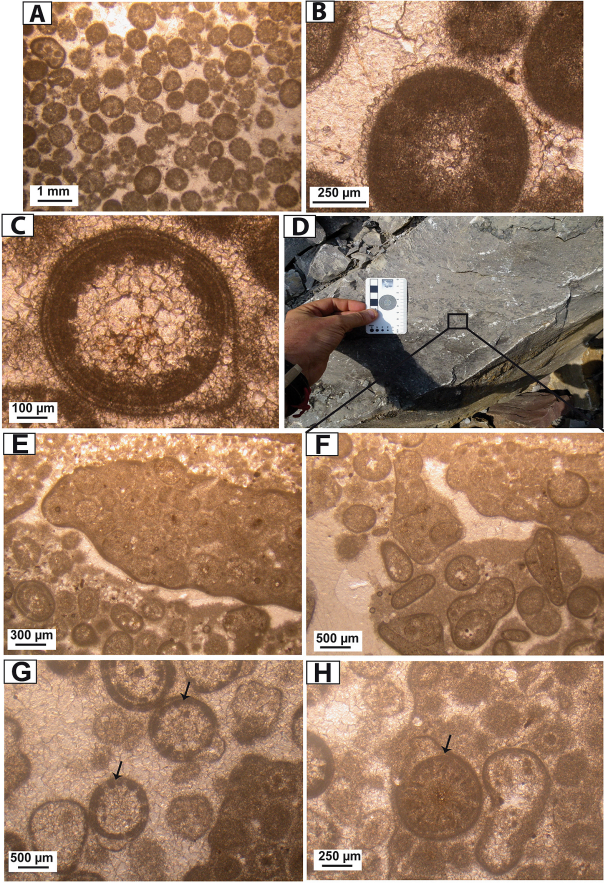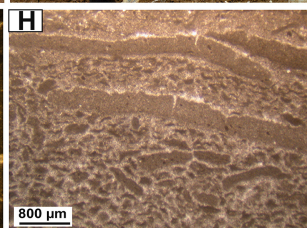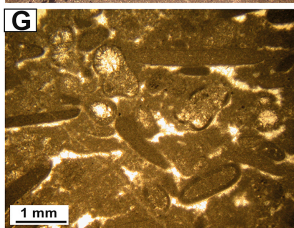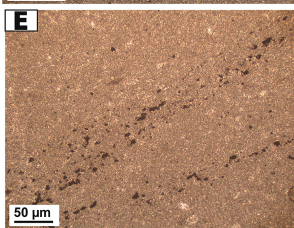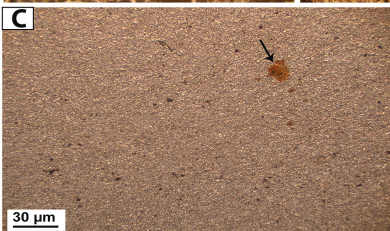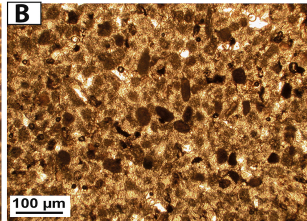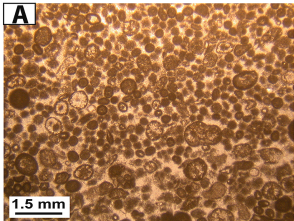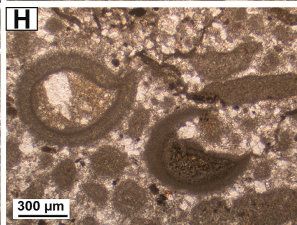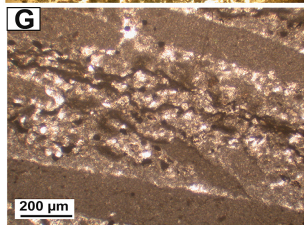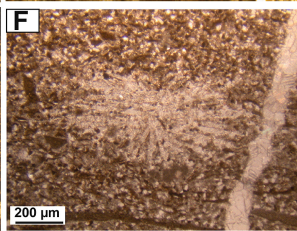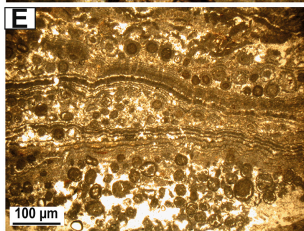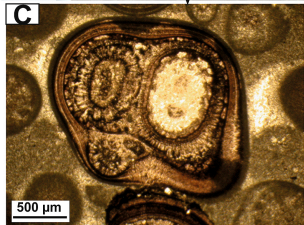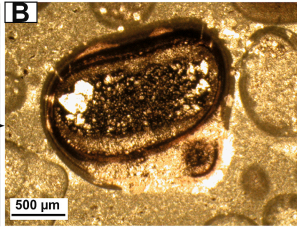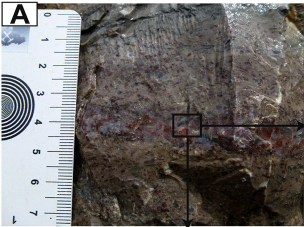
LOG (EPSG:4326 WGS 84)	Latitude	Longitude	Elevation
A	S04°06.687'	E013°54.922'	265m
B	S04°06.621'	E013°54.251'	341m
C	S04°10.824'	E013°51.076'	215m
D	S04°06.436'	E013°52.951'	321m
E	S04°06.874'	E013°51.875'	241m
F	S04°08.285'	E013°51.181'	242m
G	S04°14.720'	E013°54861'	230m
H	S04°06.517'	E013°52.372'	297m
I	S04°08.150'	E013°31.619'	196m
J	S04°04.922'	E013°30.908'	262m
K	S04°09.470'	E013°51.901'	215 m
L1	S04°03.170'	E013°06.155'	202m
M	S04°09.271'	E013°39.792'	138m
N	S04°08.965'	E013°39.493'	140m
O	S04°08.973'	E013°39.504'	140m
P	S04°08.557'	E013°40.295'	190m
Q	S04°08.266'	E013°40.397'	201m
R	S04°09.180'	E013°40.121'	153m
S	S04°09.252'	E013°40.090'	144m
T	S04°03.540'	E013°06.225'	198m
U	S04°03.119'	E013°06.282'	236m
V	S04°03.931'	E013°58.601'	446m
W	S04°03.933'	E013°58.561'	446m
X	S04°05.066'	E013°58.548'	395m
Y	S04°05.600'	E013°56.229'	371m
MAD8016 (Bitoto)	S04°04.672'	E013°31.278'	268m
MAD8019 (Zanzo)	S04°04.944'	E013°58.648'	370m
MAD8018 (Sonocc)	S04°14.720'	E013°54.861'	230m
MAD8017 (Saris)	S04°09.433'	E013°34.348'	164m

Type	Cycle features
S3	This cycle is relatively rare and less than 1.5 m-thick. The succession consists of pisoidic grainstone/floatstone, intraformational conglomerate, laminar detrital mudstone overlain by laminar microbial mats and evaporitive mudstone with abundant pseudomorphs after sulphates. Meniscus and pendular cements, keystone vugs, desiccation cracks are present. Beds are sometimes lenticular.
S2	This cycle is the most common, with thickness from a few cm to 7 m. It is a homogeneous mudstone overlain by an intraformational conglomerate, laminar detrital mudstone and topped by stratiform stromatolites, brecciated or not. Desiccation cracks, vadose cements, pseudomorphs of evaporative crystals are common. Beds are lenticular or not.
S1	Thickness varies from 0.8 m to 5 m with variable internal composition. The cycle is a succession of ooid grainstone/packstone, floatstone/packstone with abundant aggregates, peloidal grainstone/packstone, intraformational conglomerate, laminar detrital mudstone topped by stratiform stromatolites. Vadose cementation occurs. Beds must be lenticular.
D2	The cycle varies from 2 m to 10 m. The base of the cycle is a biohermal stromatolite (> 1 m) overlain by ooid grainstone/packstone or homogeneous mudstone, intraformational conglomerate, laminar detrital and by stratiform stromatolites in the top. Stromatolites show no evidence of exposure.
D1	The thickness ranges from 4 m to 20 m. The cycle is characterized by purplish laminar clayey and silty mudstones topped by giant stromatolites with no evidence of subaerial exposure.

Type	Cycle features
S3	This cycle is relatively rare and less than 1.5 m-thick. The succession consists of pisoidic grainstone/floatstone, intraformational conglomerate, laminar detrital mudstone overlain by laminar microbial mats and evaporitive mudstone with abundant pseudomorphs after sulphates. Meniscus and pendular cements, keystone vugs, desiccation cracks are present. Beds are sometimes lenticular.
S2	This cycle is the most common, with thickness from a few cm to 7 m. It is a homogeneous mudstone overlain by an intraformational conglomerate, laminar detrital mudstone and topped by stratiform stromatolites, brecciated or not. Desiccation cracks, vadose cements, pseudomorphs of evaporative crystals are common. Beds are lenticular or not.
S1	Thickness varies from 0.8 m to 5 m with variable internal composition. The cycle is a succession of ooid grainstone/packstone, floatstone/packstone with abundant aggregates, peloidal grainstone/packstone, intraformational conglomerate, laminar detrital mudstone topped by stratiform stromatolites. Vadose cementation occurs. Beds must be lenticular.
D2	The cycle varies from 2 m to 10 m. The base of the cycle is a biohermal stromatolite (> 1 m) overlain by ooid grainstone/packstone or homogeneous mudstone, intraformational conglomerate, laminar detrital and by stratiform stromatolites in the top. Stromatolites show no evidence of exposure.
D1	The thickness ranges from 4 m to 20 m. The cycle is characterized by purplish laminar clayey and silty mudstones topped by giant stromatolites with no evidence of subaerial exposure.

Saris section

The Saris section (Fig. 14) shows well-developed S2 cycles in the lower part with dominant S1 cycles in the upper part. It consists of 11 meter- to plurimeter-scale cycles with a pronounced thickening-upward trend at the fourth-order. The mean thickness is 0.85 m for the S2 cycles (ranging from 0.4-1.3 m) and is 6.5 m (ranging from 3.0-11.5 m) for the S1 cycles.

Two parasequences sets are present, the first one with S2 cycles is aggradational and the second one with S1 cycles is strongly progradational.

D section

The D section (Fig. 15) shows dominated S2 parasequences overlain by open marine D1 parasequences. It is composed of centimeter- to meter-scale facies assemblages with 73 elementary S2 parasequences and, in its upper part two plurimetric D1.

Four parasequence sets are recognized (i) aggradational 1 (minimum 4.2 m-thick) with very thin S2 cycles without thickness evolution, (ii) progradational 2 (at least 10.8 m-thick with 5 metric S2 cycles, averaging 2.2 m and ranging from 0.6-4 m), (iii) aggradational 3 with at least six S2 cycles (9.9 m-thick, averaging 1.7 m) without clear thickness evolution, (iii) aggradational 3 (at least 6.3 m-thick) and (iv) progradational 4 (± 25 m-thick) with at least two D1 cycles showing a pronounced thickening-upward evolution.

Highlights

1. The SCIc Formation records the evolution of a marine ramp

2. It is a carbonate succession of meter-scale shallowing-upward cycles

3. The cycles are the result of the interplay of relative sea-level changes

4. The SCI_c cycles are enclosed into a third-order sequence related to the deposition of the SCI

   Subgroup

Declaration of interests

☒ The authors declare that they have no known competing financial interests or personal relationships that could have appeared to influence the work reported in this paper.

☐The authors declare the following financial interests/personal relationships which may be considered as potential competing interests: